minerals

MDPI

Article

Mineralogical Characteristics of Magnetite in the Duobuza Porphyry Copper (Gold) Deposit and Their Geological Implications

Xuelian Fu [1], Changyun Gan [2], She Li [3,*], Qin Wang [1,*], Yujie Dong [2], Hongwei Xia [2], Qi Zhang [4], Rongkun Zhang [5] and Xinjuan Liang [6]

[1] College of Earth and Planetary Sciences, Chengdu University of Technology, Chengdu 610059, China; fuxuelian2024@126.com
[2] No. 5 Geological Party, Tibet Bureau of Geology and Mineral Exploration and Development, Golmud 816000, China; 17809798560@163.com (C.G.); dongyujiehb@126.com (Y.D.); xiahongwei2026@163.com (H.X.)
[3] Chinalco Tibet Jinlong Mining Co., Ltd., Lhasa 850000, China
[4] School of Earth Science and Resources, China University of Geosciences, Beijing 100083, China; hanzq497@outlook.com
[5] State Key Laboratory of Deep Earth and Mineral Exploration, Institute of Mineral Resources, Chinese Academy of Geological Sciences, Beijing 100037, China; zhangrongkun609@126.com
[6] The 2nd Geological Brigade of Sichuan, Chengdu 610041, China; 18200364261@163.com
* Correspondence: 15002915168@163.com (S.L.); wagchin@163.com (Q.W.)

Abstract

Magnetite is extensively developed within various alteration zones of the mining district. Some magnetite is closely associated with copper mineralization, possessing significant research value. The Duobuza Cu (Au) deposit is a typical porphyry-type deposit within the Bangong Co-Nujiang metallogenic belt and was the first porphyry Cu-Au deposit discovered in the Duolong copper–gold ore district. Currently, this deposit contains copper resources exceeding 3 million tons @0.46%, with associated gold resources exceeding 80 tons @0.19 g/t. This study focuses on magnetite from the Duobuza deposit. Through field geological logging and microscopic identification combined with electron microprobe analysis (EMPA) and in situ LA-ICP-MS testing, mineralogical and mineral chemical research on magnetite is conducted. This research aims to elucidate the genesis of magnetite in the Duobuza deposit and its implications for mineral exploration. Five magnetite types with different occurrences can be distinguished in the Duobuza deposit: Mt_1 is magmatic magnetite; Mt_2, Mt_3, Mt_4, and Mt_5 are hydrothermal magnetite, with Mt_5 being closely associated with copper mineralization. Mt_1 is relatively enriched in Ti, V, Al, and Cr but depleted in Mn and Si; Mt_2 is relatively enriched in Ti and Al but depleted in Si and Cr; Mt_3 is relatively enriched in Al but depleted in Mg; Mt_4 is relatively enriched in Ti, Al, V, Zn, and Mn; and Mt_5 is relatively enriched in Mg, Si, Ti, Al, Mn, and Zn but depleted in Cr. Based on the Al + Mn vs. Ti + V discrimination diagram, magnetite formed in a medium- to high-temperature environment, with hydrothermal magnetite Mt_4 forming at the lowest temperature. Vanadium (V) content can be used to estimate the oxygen fugacity (fO_2) during mineralization. Mt_1 exhibits the highest V content, indicating relatively low oxygen fugacity, whereas Mt_4 shows the lowest V content, suggesting relatively high oxygen fugacity. Mt_5 has a higher V content compared to other early-stage hydrothermal magnetites, suggesting that a lower fO_2 formation environment favors the precipitation of metal sulfides in the mining district. Trace element analysis of magnetite from the Duobuza, Bolong, and Naruo mining districts reveals that magnetite from all three deposits is enriched in Si and Al and depleted in Ca and Ni. Magmatic magnetite from the Naruo and Duobuza deposits exhibits similar elemental distribution patterns. Hydrothermal magnetite from

Check for updates

Academic Editor: Paul Alexandre

Received: 7 January 2026
Revised: 25 February 2026
Accepted: 25 February 2026
Published: 9 March 2026

Copyright: © 2026 by the authors. Licensee MDPI, Basel, Switzerland. This article is an open access article distributed under the terms and conditions of the Creative Commons Attribution (CC BY) license.

the Duobuza deposit shows significantly higher Ti and V contents compared to magnetite from the Bolong and Naruo deposits.

Keywords: Duobuza; Cu-Au deposit; porphyry; magnetite; deposit genesis

1. Introduction

The general chemical formula for magnetite is XY_2O_4, expressed as $Fe^{3+}[Fe^{2+}Fe^{3+}]O_4$ [1]. The mineralogical and mineral chemical characteristics of magnetite provide a critical window for investigating the nature of ore-forming fluids and ore-forming environments (e.g., temperature and redox state) and for discriminating deposit genesis [2]. Magnetite commonly occurs as an accessory or hydrothermal mineral in igneous, metamorphic, and sedimentary rocks. It incorporates various trace elements such as Mg, Al, Ca, Ti, V, Cr, Mn, Co and Ni [2,3]. The trace element composition of magnetite can reflect the temperature, pressure, oxygen fugacity, coexisting mineral assemblage, and composition of fluids or melts in magmatic and hydrothermal systems [1,2,4–8]. As a result, its geochemical signature serves as an effective tool for exploring ore-forming mechanisms, determining deposit genetic types, and guiding mineral exploration. With ongoing advancements in research, diagnostic physicochemical characteristics of magmatic magnetite, such as high Ti content, have been identified and utilized in studies of petrogenesis, ore formation mechanisms, deposit classification, and mineral exploration [3,9].

The Duobuza deposit is the first large porphyry Cu-(Au) deposit discovered within the Duolong ore district. Previous studies in this mining area have primarily focused on the distribution patterns of ore-forming elements, geochronology of magmatism and mineralization, sources of ore-forming materials, source and evolution of ore-forming fluids, vein characteristics, and alteration zoning patterns [10–13]. These studies have contributed to the establishment of relatively comprehensive metallogenic and exploration models [14,15], which have been instrumental in guiding deep-level and peripheral exploration efforts.

Previous mineralogical research on the Duobuza deposit has primarily focused on gangue minerals, with only Li et al. utilizing iron isotopes of hydrothermal minerals (magnetite, chalcopyrite, pyrite) in the Duobuza–Bolong area to reconstruct the evolution of magmatic–hydrothermal fluids [16]. However, detailed classification and comprehensive mineralogical–geochemical characterization of magnetite are still lacking, limiting the ability to provide precise constraints on ore-forming processes. Building on drill core logging and laboratory petrography, this study systematically investigates the mineralogy of Duobuza magnetite, establishes a classification scheme for magnetite types, summarizes their physical and chemical characteristics, and examines the trace element geochemical signatures of distinct magnetite varieties. This research provides critical mineralogical constraints for a deeper understanding of the deposit's mineralization processes and mechanisms.

2. Geological Background

2.1. Regional Geology

The Bangong Co-Nujiang metallogenic belt (BNSZ) is located in the central Tibetan Plateau (Figure 1a) [17]. In recent years, significant exploration breakthroughs have been achieved in the western segment of this belt [18]. The successive discovery and assessment of large porphyry–skarn Cu-polymetallic deposits, including those in the Duolong ore district and the Ga'erqiong–Galale ore cluster along its southern margin, as well as the Fuye and Caima deposits, have established the BNSZ as the third major Cu-polymetallic

metallogenic belt with enormous exploration potential, following the Yulong and Gangdese metallogenic belts [14,19–21].

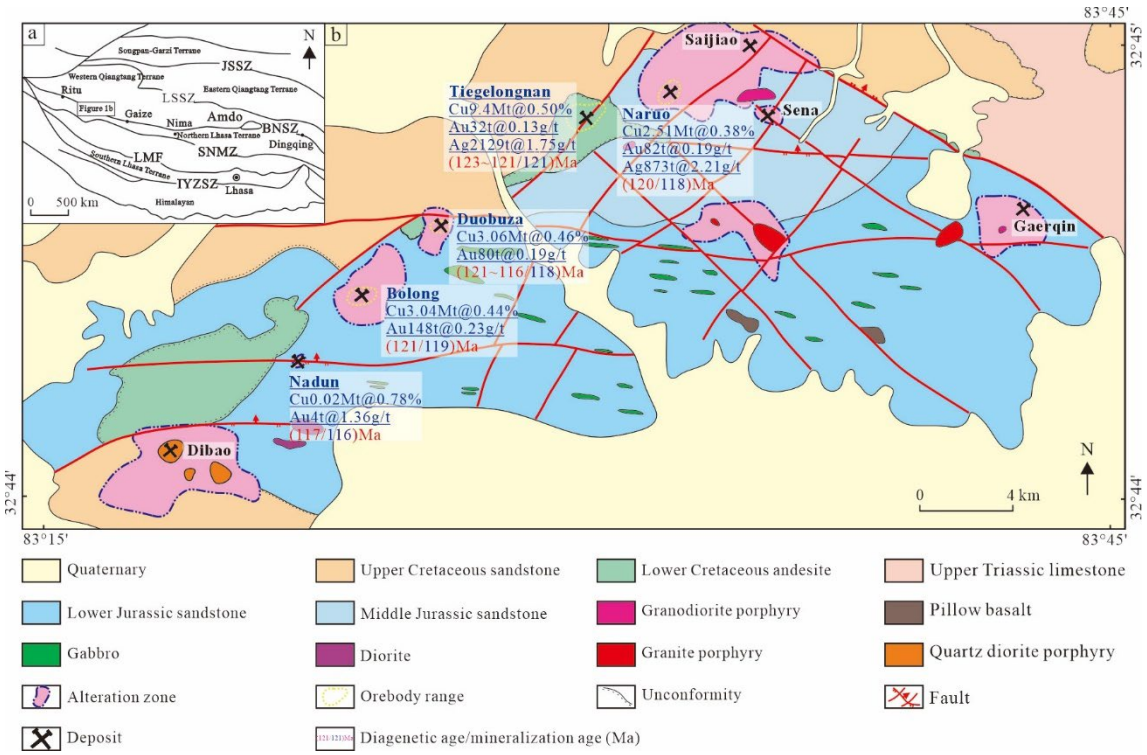


Figure 1. Outline map of the geotectonic location of the Duolong ore district (**a**) and geological map of the Duolong ore district ((**b**), modified from [22]): JSSZ—Jinsha River Suture Zone; LSSZ—Longmu–Shuanghu Suture Zone; BNSZ—Bangong Lake–Nujiang Suture Zone; SNMZ—Shiquanhe–Namucuo serpentine green mixed rock belt; LMF—Luobadui–Mila Mountain Fracture Zone; IYZSZ—India–Yaluzangbu Suture Zone.

The Duolong ore district is located on the northern flank of the western segment of the Bangong Co-Nujiang Suture Zone (BNSZ) (Figure 1a) [23]. It is characterized by Cu, Au, and other mineral resources, with primary deposit types being porphyry-type and epithermal Cu (Au) deposits [24,25]. This includes the superlarge Tiegelongnan porphyry–high-sulfidation epithermal Cu (Au) deposit [20,24]; large porphyry Cu (Au) deposits such as Duobuza, Bolong, Naruo, and Nating [20,26]; cryptoexplosive breccia pipe-type Au (Cu) deposits including Nadun and Sena [27]; high-sulfidation epithermal Cu (Au) prospects such as Dibaonamugang and Gaerqin [28–30]; as well as numerous porphyry Cu-Au prospects/mineral occurrences like Saijiao and Senadong [31] and small- to medium-sized placer Au deposits/occurrences. The estimated total copper resources exceed 25 million tons, with associated gold resources exceeding 520 tons and associated silver resources exceeding 3900 tons [32]. The geological characteristics of the major deposits and occurrences within the ore cluster area are summarized in Table 1.

The Duolong ore district exposes Mesozoic strata, including the Upper Triassic Riganpeicuo Formation marbleized limestone; the Middle–Lower Jurassic Sewa Formation metamorphosed feldspathic quartz sandstone interbedded with silty slate; the Lower Jurassic Quse Formation metamorphosed feldspathic quartz sandstone interbedded with siliceous rock, basalt, and mafic volcanic lavas; the Upper Cretaceous Abushan Formation with alternating beds of fine conglomerate, breccia, and sandstone; the Lower Cretaceous Meiriqieco Formation dominated by a volcanic assemblage of basalt, basaltic andesite, andesite, dacite, and rhyolite; the Neogene Kangtuo Formation mudstone, sandstone, and

conglomerate; and Quaternary deposits [22,25,26,33,34]. Among these, feldspathic quartz sandstone serves as the main host rock for mineralization within the ore district [21].

Magmatic activity in the ore district was concentrated during the Early Cretaceous (123~105 Ma) [35], predominantly manifesting as volcanic eruptions, effusions, and hypabyssal intrusions [30]. Mafic, intermediate-acidic, and acidic rock bodies are exposed, generally of small scale, typically distributed in linear or beaded patterns, occurring in clusters with evident structural control by fault systems, and exhibiting multiphase emplacement characteristics [30,33]. The intrusive rocks consist mainly of granodiorite porphyry and quartz diorite porphyry, while the volcanic rocks are dominated by basaltic andesite and andesite, among others. The basalt formed slightly earlier (143 Ma) [36], whereas the andesites are relatively younger. Notably, the granodiorite porphyry serves as the primary ore-bearing intrusion in the area [23,25].

Fault structures are well-developed within the ore district, predominantly comprising three sets trending EW, NE, and NW. These faults dissect the Duolong ore district into a diamond-shaped structural framework (Figure 1b), demonstrating long-term and polyphase activity. The EW-trending faults serve as the primary structures controlling magmatism and mineralization. Among these, an E-W-striking thrust fault (150~200 m wide) developed in the central sector along the Duobuza deposit displays pervasive cataclasis within the fault zone, with observed tectonic breccia composed of andesitic rocks. This structure is disrupted and displaced by later NW- and NE-trending faults, resulting in discontinuity [17,34]. NE-trending faults postdate the EW-trending system. Areas where NE- and EW-trending faults intersect constitute favorable exploration targets. NW-trending faults represent the youngest fault set in the area, which cross-cut NE-trending faults and act as ore-disrupting structures [22].

Table 1. Geological characteristics of principal deposits and occurrences in the Duolong ore district.

Deposit	Deposit Type	Scale	Host Rock	Alteration	Metallic Minerals	Reserves	Grade	Reference
Bolong	Porphyry	Large	Granodiorite Porphyry, Feldspathic Quartz Sandstone	Potassic Alteration, Phyllic Alteration, Propylitic Alteration	Chalcopyrite, Bornite, Pyrite, Magnetite, Molybdenite	Cu: 4.75 Mt Au: 230.4 tons	Cu: 0.44% Au: 0.23 g/t	[37,38]
Duobuza	Porphyry	Large	Granodiorite Porphyry, Feldspathic Quartz Sandstone	Potassic Alteration, Phyllic Alteration, Propylitic Alteration	Chalcopyrite, Bornite, Tetrahedrite, Pyrite, Molybdenite, Magnetite	Cu: 3.48 Mt Au: 88.2 tons	Cu: 0.46% Au: 0.19 g/t	[13,35,36]
Tiegelongnan	Porphyry–Epithermal	Giant	Granodiorite Porphyry, Diorite Porphyrite, Feldspathic Quartz Sandstone	Weak Potassic Alteration, Phyllic Alteration, Propylitic Alteration, Advanced Argillic Alteration	Chalcopyrite, Bornite, Covellite, Digenite, Enargite, Pyrite, Molybdenite	Cu: 9.78 Mt Au: 28.9 tons Ag: 12.24 tons	Cu: 0.51% Au: 0.13 g/t Ag: 1.80 g/t	[21,24,30]
Naruo	Porphyry-Related Cryptoexplosive Breccia	Large	Granodiorite Porphyry, Feldspathic Quartz Sandstone	Weak Potassic Alteration, Weak Phyllic Alteration, Propylitic Alteration	Chalcopyrite, Bornite, Pyrite, Magnetite	Cu:2.7 Mt Au: 80 tons Ag: 2000 tons	Cu: 0.38% Au: 0.18 g/t Ag: 1.72 g/t	[26,31]

Table 1. *Cont.*

Deposit	Deposit Type	Scale	Host Rock	Alteration	Metallic Minerals	Reserves	Grade	Reference
Nating	Porphyry	Large	Granodiorite Porphyry, Feldspathic Quartz Sandstone	Silicification, Phyllic Alteration, Clay Alteration	Chalcopyrite, Pyrite, Magnetite	Cu: 1.05 Mt Au: 80 tons	Cu: 0.31% Au: 0.25 g/t	[31,39]
Nadun	Porphyry-Related Cryptoexplosive Breccia	Small	Cryptoexplosive Breccia Pipe	Silicification, Phyllic Alteration, Clay Alteration	Chalcopyrite, Pyrite, Bornite, Digenite, Galena, Sphalerite			[27]
Sena	Porphyry	Mineral Occurrence	Quartz Monzodiorite, Granodiorite Porphyry	Silicification, Sericitic Alteration, Carbonatization, Clay Alteration	Chalcopyrite, Pyrite			[40]
Saijiao	Porphyry	Mineral Occurrence	Granodiorite Porphyry	Silicification, Sericitic Alteration, Weak Clay Alteration	Chalcopyrite, Pyrite, and Minor Magnetite			[41]
Dibao	Porphyry–Epithermal	Small	Granite Porphyry, Granodiorite Porphyry, Feldspathic Quartz Sandstone	Intense Argillic Alteration, Phyllic Alteration, Weak Silicification	Pyrite, Minor Chalcopyrite and Magnetite			[29]
Gaerqin	Porphyry	Small	Granodiorite Porphyry	Intense Silicification, Sericitic Alteration, Weak Clay Alteration	Chalcopyrite, Pyrite			[28,42]
Tiegeshan	Porphyry	Mineral Occurrence	Granodiorite Porphyry	Intense Silicification, Sericitic Alteration, Clay Alteration	Pyrite, Minor Chalcopyrite			[24]

2.2. Deposit Geology

2.2.1. Geological Characteristics

The stratigraphic sequence in the Duobuza mining area predominantly consists of the Upper Cretaceous Abushan Formation (K_2a) and the Lower Cretaceous Meiriqiecuo Formation (K_1m), with additional exposures of the Mugagangri Formation (JM) and Quaternary deposits (Q) [12,22].

Two major fault structures, F2 and F14, are present in the mining area, with secondary fracture structures commonly developed around the periphery of these main faults [35]. The F2 fault trends approximately E-W in the northern part of the mining area, with its fault plane dipping southward at an angle of approximately 65° (Figure 2). This structure thrusts the Duobuza ore-bearing porphyry and orebody over the Upper Cretaceous Abushan Formation sandstone conglomerate, forming the northern boundary of the orebody and exhibiting typical characteristics of a post-mineralization fault that disrupts the orebody [35,36]. The F14 fault is located in the northwest of the mining area and trending NW is also a post-mineralization structure (Figure 2).

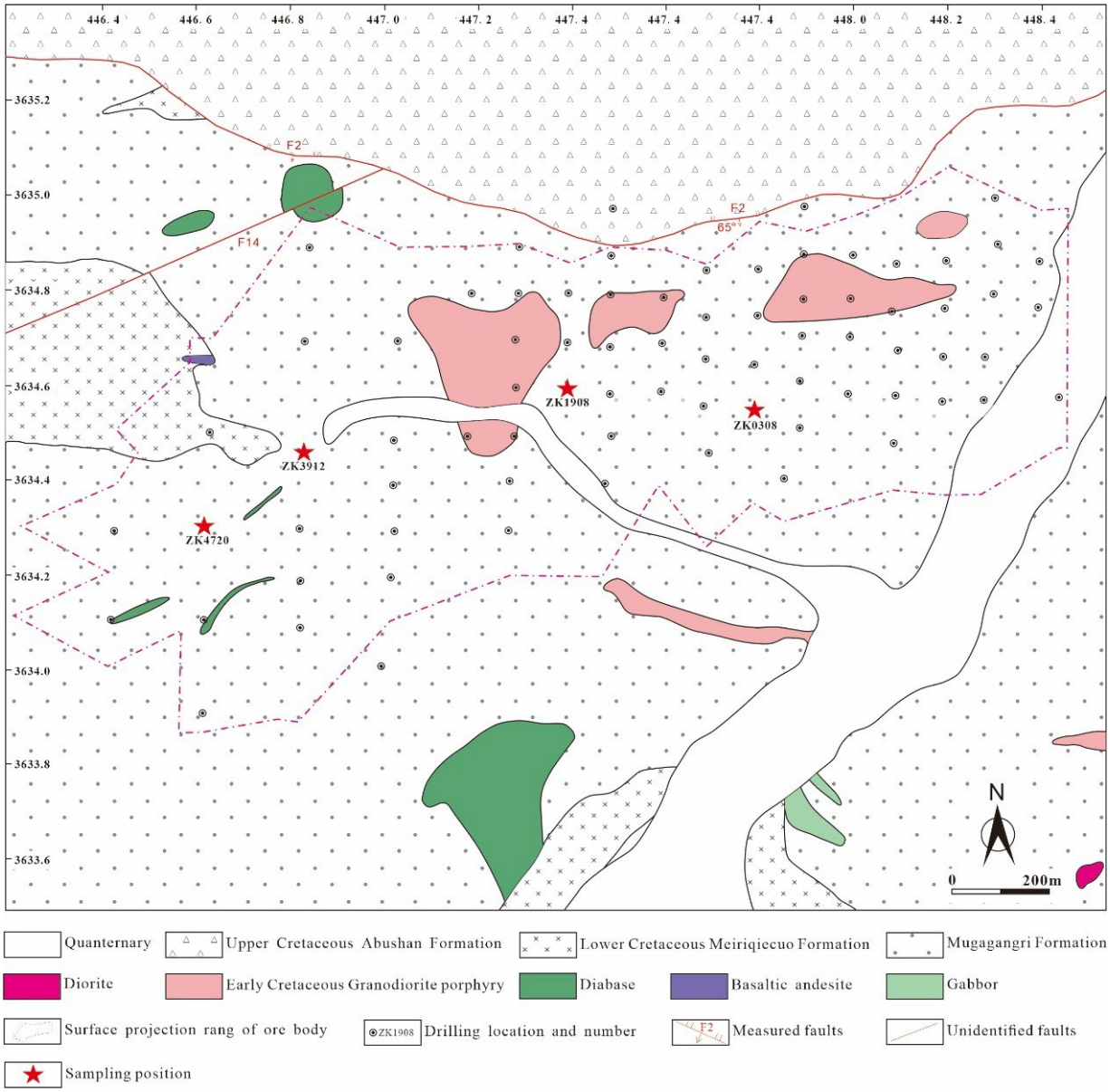


Figure 2. Geological map of the Duobuza porphyry copper (gold) deposit.

Magmatic activity within the area is complex and characterized by multiple phases, including the intrusion of granodiorite porphyry, diabase, gabbro, and basaltic andesite, primarily occurring as stocks and dikes [14]. The primary ore-bearing rock is granodiorite porphyry, mainly exposed in the northeastern and southwestern parts of the mining area [11]. Mineralization is primarily developed within the granodiorite porphyry and its contact zone with the surrounding rocks. The granodiorite porphyry serves as the main ore-bearing intrusion, with feldspathic quartz sandstone being the principal intrusive wall rock.

The Duobuza deposit displays a characteristic zonation pattern extending outward from the porphyry stock: potassic alteration zone (overprinted peripherally by argillic and sericitic alteration) → phyllic alteration zone (largely overprinted by argillic alteration) → propylitic alteration zone → hornfels zone [13], demonstrating the typical alteration zoning of a porphyry deposit (Figure 3).

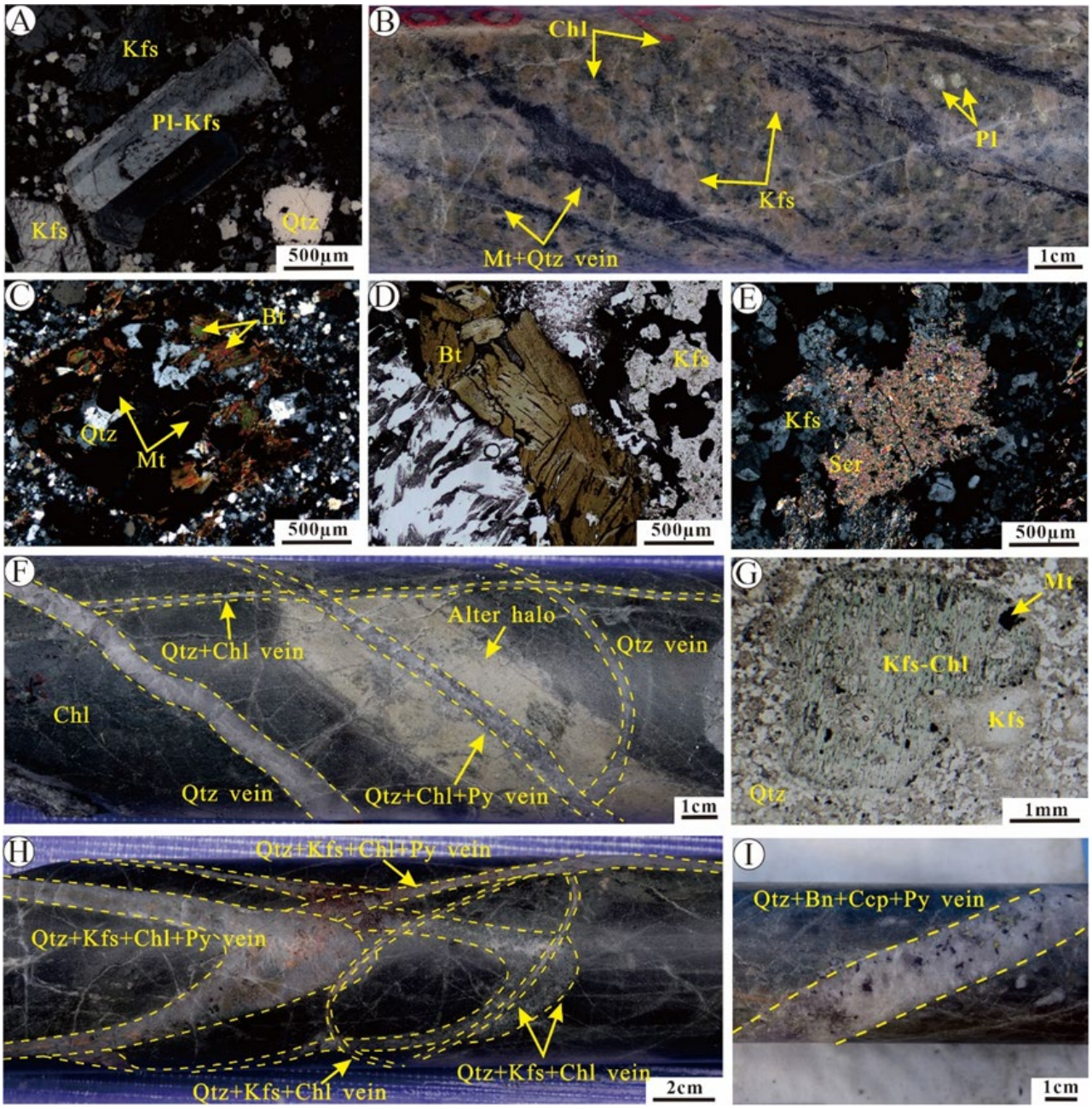


Figure 3. Representative photographs illustrating the characteristics of the alteration zones: (**A**) DBZK3912—649.2 m: plagioclase replaced by K-feldspar; (**B**) DBZK1908—575.75 m: magnetite + quartz vein within potassic alteration zone, and primary K-feldspar exhibiting characteristic pinkish hue; (**C**) DBZK3912—649.2 m: hornblende replaced by biotite; (**D**) DBZK3912—299.83 m: hydrothermal biotite vein; (**E**) DBZK3912—299.83 m: sericitization; (**F**) DBZK1908—415.5 m: chloritization overprinting phyllic alteration zone, with development of quartz veins, quartz + chlorite veins, and quartz + chlorite + pyrite veins, surrounded by chlorite alteration halos; (**G**) DBZK3912—433.82 m: K-feldspar replaced by chlorite; (**H**) DBZK1908—425.1 m: mutual cross-cutting relationships between quartz + K-feldspar + chlorite veins and quartz + K-feldspar + chlorite + pyrite veins; (**I**) DBZK3912—323.5 m: quartz + bornite + chalcopyrite + pyrite vein cross-cutting early hornfelsed alteration. Qtz—quartz; Kfs—K-feldspar; Pl—plagioclase; Mt—magnetite; Bt—biotite; Ccp—chalcopyrite; Py—pyrite; Bn—bornite; Chl—chlorite; Ser—sericite.

The potassic alteration zone is predominantly located in the central part of the deposit. The alteration minerals primarily include K-feldspar, biotite, and quartz, dominated by biotitization and K-feldspar alteration. K-feldspar alteration is primarily characterized

by secondary K-feldspar replacing primary plagioclase (Figure 3A). Minor primary K-feldspar is also observed, appearing flesh-red (Figure 3B). Biotitization is characterized by secondary biotite replacing hornblende (Figure 3C) or occurring as biotite hydrothermal veins (Figure 3D). Due to subsequent phyllic alteration overprinting the potassic alteration, biotite is replaced by sericite, making it difficult to identify. This zone hosts disseminated chalcopyrite mineralization and minor pyrite mineralization, with veins including quartz + K-feldspar veins, K-feldspar stringers, magnetite + quartz veins (Figure 3B), and quartz + chalcopyrite + gypsum veins.

The phyllic alteration zone is characterized by principal alteration minerals such as sericite, quartz, pyrite, etc. (Figure 3E). Veins of quartz + chalcopyrite + pyrite and quartz + chlorite + pyrite are well developed within this zone (Figure 3F). Copper mineralization gradually weakens from the center towards the periphery.

The propylitic alteration zone is located outward from the phyllic alteration zone, with major alteration minerals including epidote, chlorite, calcite, etc. Minor pyrite is also present within this zone. Chlorite primarily replaces biotite and hornblende, occurring as patchy aggregates while often retaining the crystal form of the original mineral (Figure 3G). Epidotization is observed within basaltic andesite on the western side of the mining area and in some volcanic breccias on the southern side. The propylitic alteration zone develops as discontinuous patches within the deposit, failing to form a continuous ring.

The hornfels zone exhibits sparse-disseminated magnetite and biotite which are visible on the core surface. Veins of quartz + pyrite, quartz + chalcopyrite + bornite, quartz + magnetite, and quartz + pyrite + chalcopyrite are developed, with vein widths ranging from 0.1 cm to 2 cm. Vein cross-cutting relationships are complex; for example, quartz + K-feldspar + chlorite veins and quartz + K-feldspar + chlorite + pyrite veins mutually cross-cut each other (Figure 3H), or quartz–sulfide veins cut through the hornfelsed alteration (Figure 3I).

2.2.2. Mineralization

Mineralization at the Duobuza deposit primarily occurs within the ore-bearing porphyry and its contact zone with the surrounding rocks. Mineralization is closely associated with the potassic alteration zone. Ore minerals are dominated by chalcopyrite, followed by pyrite, molybdenite, bornite, tetrahedrite, sphalerite, magnetite, hematite, pyrrhotite, and siderite (Figure 4A–G). Gangue minerals primarily consist of K-feldspar, plagioclase, quartz, biotite, sericite, muscovite, chlorite, epidote, calcite, gypsum, kaolinite, and halloysite (Figure 4H–L). Ore textures are predominantly veinlet and disseminated. Based on field geological surveys and petrographic observations, two distinct stages of mineralization, namely magmatic and hydrothermal, have been identified (Figure 5). The generations of mineral formation are differentiated based on mineral chemical composition, structural features, morphological characteristics, and cross-cutting relationships within the vein system. The hydrothermal stage can be further subdivided into the potassic alteration stage, sericitization stage, chloritization stage, and sulfide vein stage.

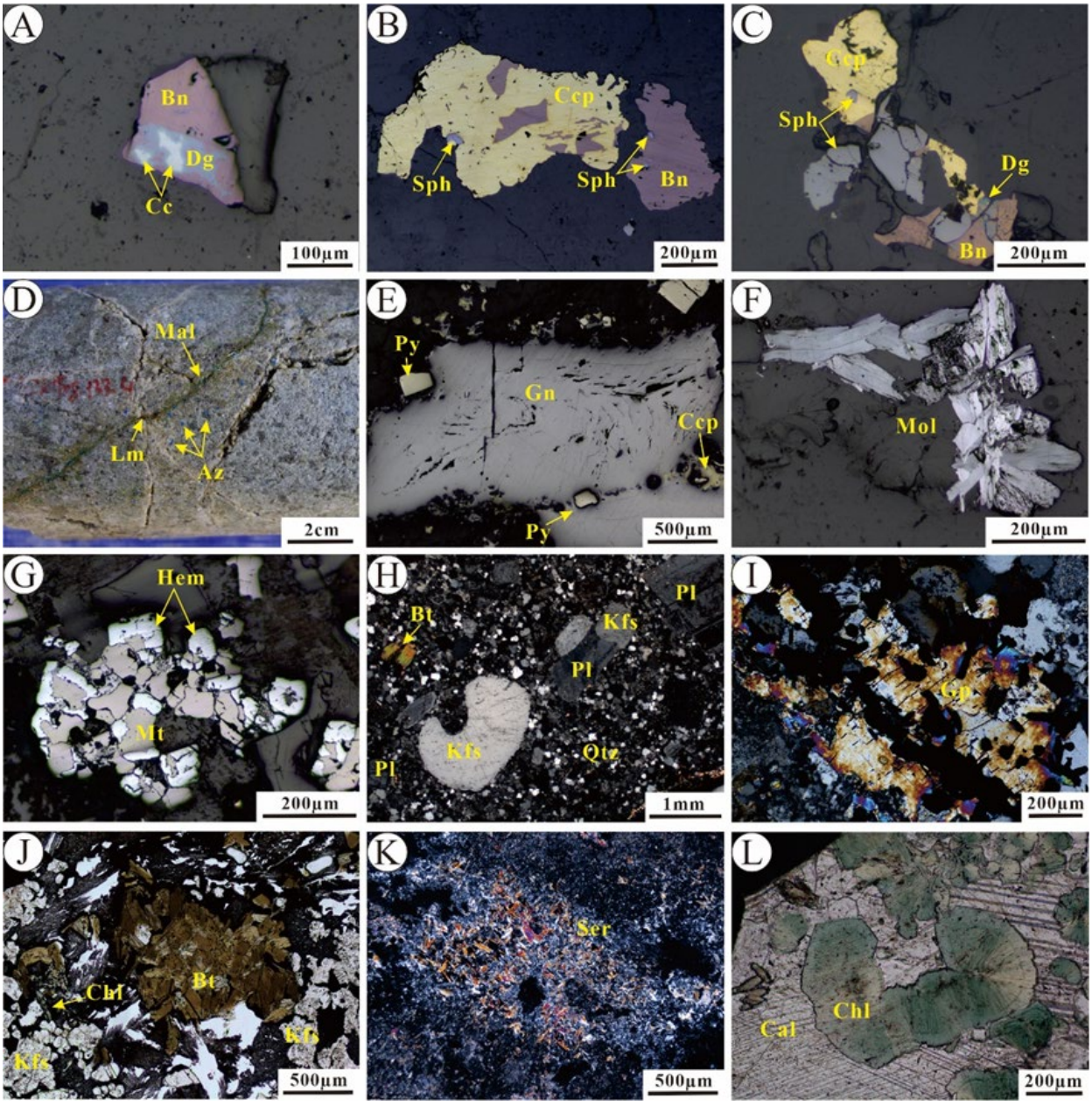


Figure 4. Representative photomicrographs illustrating the characteristics of ore minerals: (**A**) DBZK3912—369.22 m: intergrowth of bornite, digenite, and chalcocite; (**B**) DBZK3912—597.6 m: chalcopyrite, bornite and sphalerite assemblage; (**C**) DBZK3912—369.22 m: chalcopyrite and sphalerite assemblage with digenite replacing bornite along margins and fractures; (**D**) DBZK1908—133.4 m: azurite occurring as patchy aggregates, with hematite and malachite along fractures; (**E**) DBZK1908—687.5 m: galena showing cubic cleavage and euhedral pyrite; (**F**) DBZK0308—117 m: bireflectance of molybdenite; (**G**) DBZK4720—493.7 m: hematite replacing magnetite with reaction rims; (**H**) DBZK3912—649.2 m: phenocrysts of K-feldspar, plagioclase, and biotite in granodiorite porphyry; (**I**) DBZK4720—517.8 m: anhedral gypsum; (**J**) DBZK3912—299.83 m: hydrothermal biotite; (**K**) DBZK3912—597.6 m: sericitization; (**L**) DBZK3912—580.2 m: fan-shaped chlorite intergrown with calcite. Dg—digenite, Cc—chalcocite, Mal—malachite, Az—azurite, Lm—limonite, Ccp—chalcopyrite, Py—pyrite, Bn—bornite, Sph—sphalerite, Gn—galena, Mol—molybdenite, Mt—magnetite, Hem—hematite, Pl—plagioclase, Kfs—K-feldspar, Qtz—quartz, Bt—biotite, Chl—chlorite, Ser—sericite, Cal—calcite, Gp—gypsum.

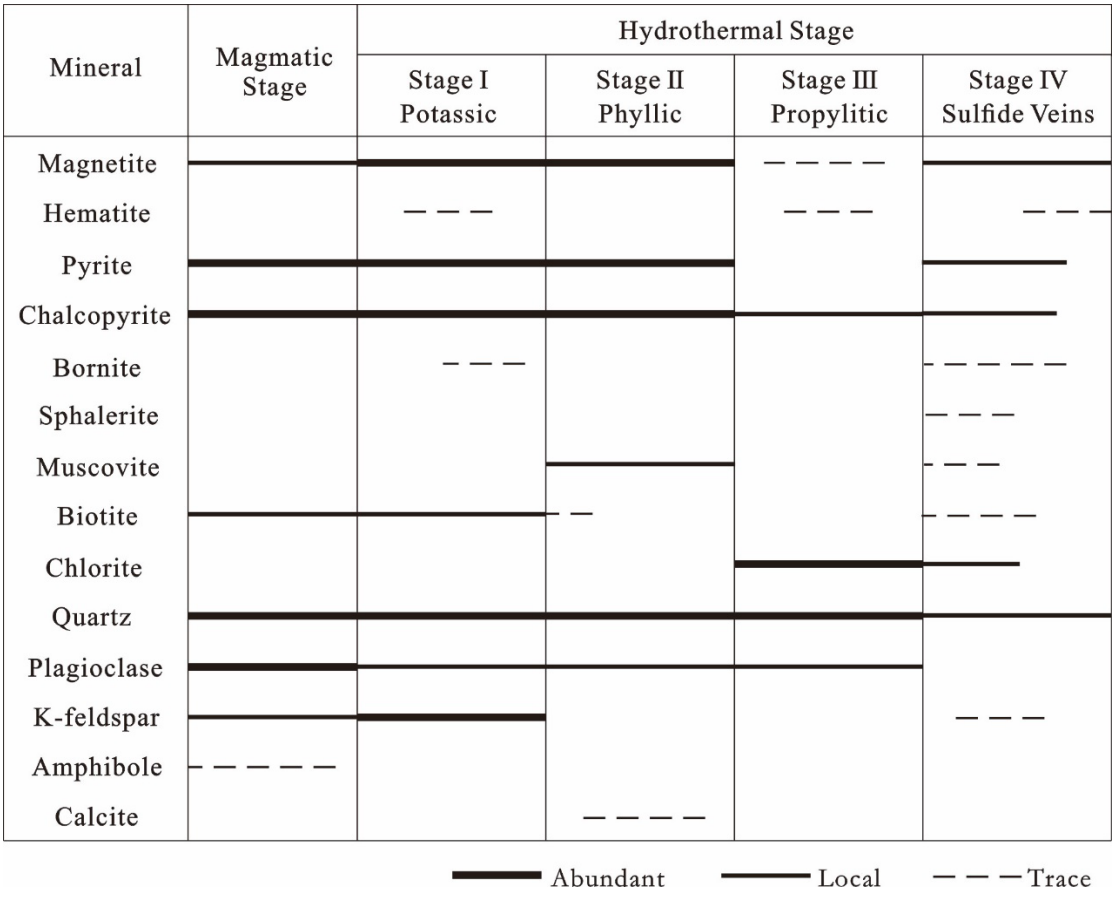


Figure 5. Mineral formation sequence in the Duobuza porphyry (gold) deposit.

3. Mineralogy of Magnetite

In the Duobuza deposit, abundant magnetite develops within the potassic alteration zone, phyllic alteration zone, propylitic alteration zone, and hornfels zone. From the center of the porphyry body outward to the periphery, magnetite gradually decreases in abundance. Its texture transitions progressively from dense-disseminated and patchy/disseminated to disseminated and sparse-disseminated. Additionally, magnetite occurs in vein-type forms, predominantly as quartz–magnetite veins and quartz–magnetite veins ± chalcopyrite ± pyrite. Magnetite is closely associated with abundant sulfides. The Duobuza deposit can be classified into five types of magnetite with distinct modes of occurrence:

(1) Mt_1: Primarily occurs as disseminated or dense-disseminated in granodiorite porphyry (Figure 6A). Microscopically, it shows irregular granular forms with a gray-white reflective color, with the magnetite diameter ranging from approximately 100 μm to 1.5 mm. It commonly coexists with quartz and K-feldspar (Figure 6B,C).

(2) Mt_2: Mainly occurs in granodiorite porphyry (Figure 6D). Microscopically, it displays subrounded granular forms, with a smoother surface than Mt_1, and a light gray reflective color. The magnetite diameter is about 50 μm to 1 mm, with some magnetite enclosed by chlorite or biotite (Figure 6E,F), and occasionally contains chalcopyrite and bornite.

(3) Mt_3: Mainly occurs as a sparsely disseminated form (Figure 6G). The magnetite diameter ranges from 30 to 600 μm, displaying a pinkish-brown reflective color. It typically coexists with quartz, gypsum, and chlorite and contains minor chalcopyrite. This magnetite is commonly replaced by hematite at the margins (Figure 6H,I).

(4) Mt_4: Mainly occurs in the hornfelsized alteration zone as sparsely a disseminated form (Figure 6J), exhibiting a pinkish-brown reflective color and sub-square or irregular granular shapes. The magnetite diameter ranges from 10 to 80 μm and it typically coexists with quartz, muscovite, chlorite (Figure 6K,L).

(5) Mt_5: Mainly occurs in feldspathic quartz sandstone, typically as magnetite veins, quartz–magnetite veins, clay mineral–magnetite veins, and quartz–pyrite–chalcopyrite–magnetite veins (Figure 6M). Microscopically, it has a dark gray color and commonly coexists with quartz, with its grain fracture surfaces hosting pyrite and chalcopyrite (Figure 6N,O).

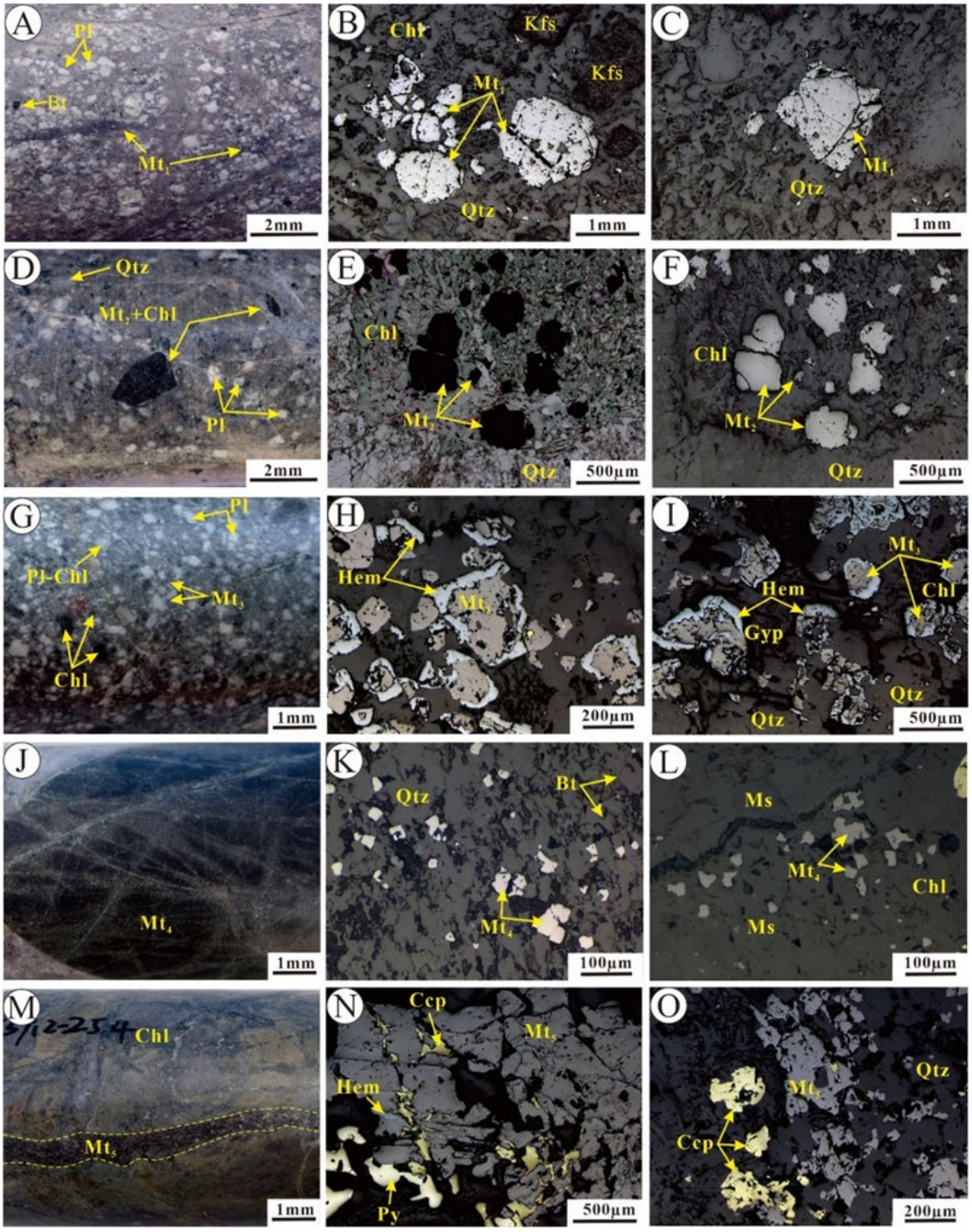


Figure 6. Hand specimen and photomicrographs illustrating distinctive characteristics of magnetite: (**A**) DBZK3912—309.4 m, magnetite disseminated in granodiorite porphyry; (**B**) DBZK3912—433.82 m,

magnetite coexists with quartz and chlorite; (**C**) DBZK3912—433.82 m, magnetite coexists with quartz; (**D**) DBZK1908—368.7 m, magnetite in granodiorite porphyry enclosed by chlorite; (**E**) DBZK1908—350.3 m, magnetite enclosed by chlorite; (**F**) DBZK1908—350.3 m, magnetite enclosed by chlorite; (**G**) DBZK1908—256.35 m, magnetite occurs as sparsely disseminated form; (**H**) DBZK3912—525.25 m, magnetite margins replaced by hematite; (**I**) DBZK3912—525.25 m, magnetite margins replaced by hematite, coexisting with chlorite, gypsum, and quartz; (**J**) DBZK3912—576.6 m, disseminated magnetite in hornfels; (**K**) DBZK3912—369.22 m, magnetite coexists with quartz and biotite; (**L**) DBZK3912—369.22 m, magnetite coexists with muscovite and chlorite; (**M**) DBZK3912—25.4 m, magnetite–quartz–pyrite–chalcopyrite vein; (**N**) DBZK4720—517 m, magnetite coexists with chalcopyrite and pyrite, with partial margins replaced by hematite; (**O**) DBZK3912—525.25 m, magnetite coexists with chalcopyrite and quartz. Qtz—quartz; Kfs—K-feldspar; Pl—plagioclase; Mt—magnetite; Bt—biotite; Ccp—chalcopyrite; Py—pyrite; Bn—bornite; Hem—hematite; Ms—muscovite; Gyp—gypsum; Chl—chlorite.

4. Samples and Methods

4.1. Samples

Based on detailed geological investigations, systematic geological logging was conducted on drill cores from the Duobuza mining area. Samples for this study were collected from various altered rocks, including drill holes DBZK1908, DBZK0308, DBZK3912, and DBZK4720 (Figure 2). Among them, magnetite in granodiorite porphyry mainly occurred as disseminated and patchy (Figure 6A,D), magnetite in feldspathic quartz sandstone occurred as disseminated and vein-type (quartz–magnetite veins, quartz–pyrite–magnetite veins) (Figure 6G,M), and magnetite in hornfels mostly occurred as sparsely disseminated (Figure 6J). Thirteen magnetite samples were collected from granodiorite porphyry, 17 magnetite samples were collected from feldspathic quartz sandstone, and 4 magnetite samples were collected from hornfels. For collected rock samples, polished thin sections were prepared, and based on detailed microscopic identification, representative magnetite samples were selected for electron probe microanalysis (EPMA) testing and LA-ICP-MS in situ analysis.

4.2. Methods

This electron probe microanalysis (EPMA) testing was completed in the EPMA laboratory of Institute of Mineral Resources, Chinese Academy of Geological Sciences. The EPMA laboratory of Institute of Mineral Resources, Chinese Academy of Geological Sciences, used testing instrument model JXA-8230 (manufactured by JEOL, Akishima City, Japan), with the following operating conditions: 15 kV; electron beam current 20 nA; beam diameter 1~5 μm; and peak positioning time 10 s. Detection limits: F (1098~1174) ppm, Na (71~87) ppm, Al (77~81) ppm, Mg (65~74) ppm, Si (83~96) ppm, Ti (236~244) ppm, Mn (104~113) ppm, Cr (112~137) ppm, Ni (136~154) ppm, Fe (87~99) ppm, V (104~192) ppm, K (48~53) ppm, and Ca (64~77)ppm. This experiment completed 68 EPMA test points and measured major element data (Na, Al, Mg, Si, Ti, Mn, Cr, Ni, Fe, V, K, Ca). For details, see Table 2.

Table 2. Electron probe microanalyzer (EPMA) data (%) for magnetite of different occurrences from the Duobuza porphyry Cu (-Au) deposit.

Sample	Type	Na_2O	Al_2O_3	MgO	SiO_2	TiO_2	MnO	Cr_2O_3	NiO	V_2O_5	K_2O	CaO	FeO	Total
ZK0308-467.6-1	Mt_1	0.02	0.60	0.01	0.65	0.38	0.00	0.03	0.00	0.33	0.00	0.03	92.85	94.90
ZK0308-467.6-2	Mt_1	0.00	0.88	0.06	0.59	0.40	0.15	0.03	0.00	0.30	0.00	0.01	92.00	94.41
ZK0308-467.6-3	Mt_1	0.00	0.87	0.08	0.48	0.49	0.21	0.03	0.00	0.29	0.00	0.00	92.83	95.27
ZK0308-467.6-4	Mt_1	0.01	0.81	0.06	0.73	0.53	0.10	0.05	0.00	0.30	0.00	0.02	91.98	94.58
ZK0308-478.9-2	Mt_1	0.00	0.43	0.05	0.90	0.23	0.15	0.06	0.00	0.30	0.00	0.02	92.19	94.33
ZK1908-215.5-1	Mt_1	0.00	0.27	0.04	1.15	0.22	0.08	0.04	0.00	0.37	0.00	0.01	91.75	93.94
ZK1908-215.5-2	Mt_1	0.00	0.50	0.02	0.91	0.16	0.06	0.07	0.00	0.36	0.00	0.00	91.41	93.48
ZK1908-215.5-4	Mt_1	0.00	0.21	0.04	1.18	0.13	0.07	0.01	0.00	0.30	0.00	0.01	91.73	93.67
ZK1908-257(2)-4	Mt_1	0.00	0.57	0.00	0.55	0.23	0.08	0.04	0.00	0.58	0.00	0.01	92.02	94.08
ZK1908-350.3-3	Mt_1	0.01	0.79	0.07	0.50	0.29	0.05	0.05	0.00	0.35	0.00	0.05	92.49	94.67
ZK1908-456.4-1	Mt_1	0.00	0.62	0.00	0.48	0.34	0.03	0.17	0.00	0.73	0.00	0.00	92.81	95.19
ZK1908-456.4-2	Mt_1	0.00	0.53	0.05	0.79	0.24	0.04	0.18	0.00	0.67	0.02	0.01	92.59	95.12
ZK1908-587.1-1	Mt_1	0.01	0.59	0.02	0.70	0.35	0.14	0.19	0.00	0.24	0.00	0.02	91.49	93.76
ZK1908-635.9-2	Mt_1	0.01	0.52	0.04	0.71	0.36	0.11	0.01	0.00	0.43	0.00	0.01	93.09	95.30
Average		0.00	0.59	0.04	0.74	0.31	0.09	0.07	0.00	0.40	0.00	0.01	92.23	94.48
ZK0308-478.9-1	Mt_2	0.00	0.60	0.04	0.85	0.33	0.08	0.08	0.00	0.42	0.00	0.01	91.21	93.64
ZK1908-222.7-1-2	Mt_2	0.00	1.31	0.08	0.69	0.28	0.10	0.13	0.00	0.17	0.00	0.02	91.61	94.37
ZK1908-333.2-2	Mt_2	0.01	0.75	0.08	0.60	0.22	0.14	0.01	0.00	0.23	0.00	0.02	91.71	93.77
ZK1908-350.3-1	Mt_2	0.00	0.83	0.03	0.67	0.28	0.00	0.01	0.00	0.26	0.00	0.01	92.98	95.07
ZK1908-350.3-2	Mt_2	0.00	0.70	0.05	0.67	0.66	0.06	0.01	0.00	0.22	0.00	0.00	92.13	94.51
ZK1908-576.5-1-2	Mt_2	0.01	0.81	0.03	0.77	0.43	0.12	0.01	0.00	0.22	0.00	0.00	92.60	94.99
ZK1908-576.5-2-1	Mt_2	0.00	0.70	0.07	0.56	0.37	0.15	0.04	0.00	0.17	0.00	0.01	91.81	93.86
ZK1908-576.5-2-2	Mt_2	0.01	0.74	0.02	0.66	0.44	0.04	0.04	0.00	0.19	0.00	0.02	92.73	94.89
ZK1908-576.5-2-3	Mt_2	0.01	0.82	0.12	0.54	0.34	0.23	0.05	0.00	0.46	0.02	0.02	91.19	93.78
ZK1908-587.1-2	Mt_2	0.00	1.06	0.02	0.81	0.36	0.25	0.21	0.00	0.31	0.05	0.03	91.77	94.86
ZK1908-610.5-3	Mt_2	0.00	0.74	0.03	0.34	0.34	0.06	0.05	0.00	0.29	0.00	0.01	93.97	95.81
ZK1908-635.9-1	Mt_2	0.02	0.75	0.03	0.72	0.51	0.14	0.00	0.00	0.19	0.00	0.07	92.82	95.25
ZK1908-654.9-1	Mt_2	0.00	0.74	0.03	0.72	0.40	0.11	0.05	0.00	0.23	0.00	0.01	92.19	94.48
ZK1908-654.9-2	Mt_2	0.01	0.77	0.05	0.63	0.56	0.17	0.03	0.00	0.23	0.00	0.00	91.89	94.34
ZK1908-654.9-3	Mt_2	0.09	0.79	0.13	0.86	0.33	0.15	0.19	0.00	0.22	0.00	0.01	90.87	93.63
ZK1908-584.15	Mt_2	0.00	0.42	0.04	0.59	0.30	0.09	0.19	0.00	0.47	0.00	0.00	92.25	94.34
ZK3912-473.42-2-1	Mt_2	0.00	0.12	0.04	0.03	0.21	0.11	0.10	0.00	0.44	0.00	0.00	91.77	92.81
ZK3912-473.42-3	Mt_2	0.00	0.11	0.00	0.07	0.24	0.01	0.06	0.12	0.45	0.00	0.00	92.21	93.27
Average		0.01	0.71	0.05	0.60	0.37	0.11	0.07	0.01	0.29	0.00	0.01	92.09	94.32

Table 2. *Cont.*

Sample	Type	Na_2O	Al_2O_3	MgO	SiO_2	TiO_2	MnO	Cr_2O_3	NiO	V_2O_5	K_2O	CaO	FeO	Total
ZK1908-191.6	Mt_3	0.00	0.42	0.03	1.14	0.20	0.17	0.02	0.00	0.23	0.00	0.01	91.74	94.50
ZK1908-198.6-1	Mt_3	0.01	0.31	0.02	0.83	0.20	0.04	0.02	0.00	0.26	0.00	0.01	92.48	94.69
ZK1908-198.6-2	Mt_3	0.02	0.30	0.00	0.69	0.19	0.12	0.00	0.00	0.18	0.02	0.00	93.88	95.39
ZK1908-215.5-3	Mt_3	0.00	0.36	0.02	0.93	0.12	0.01	0.01	0.00	0.27	0.00	0.01	91.07	92.79
ZK1908-222.7-1-1	Mt_3	0.01	0.55	0.04	0.54	0.09	0.11	0.01	0.00	0.27	0.00	0.00	93.03	94.64
ZK1908-257(1)-2	Mt_3	0.01	0.55	0.05	0.77	0.21	0.17	0.03	0.00	0.11	0.00	0.01	92.79	94.68
ZK1908-257(1)-3	Mt_3	0.00	0.36	0.03	1.07	0.20	0.08	0.04	0.00	0.17	0.00	0.02	92.06	94.02
ZK1908-257(2)-1	Mt_3	0.00	0.55	0.07	0.83	0.14	0.17	0.00	0.00	0.14	0.00	0.00	90.83	92.74
ZK1908-323.9	Mt_3	0.02	0.49	0.02	0.64	0.67	0.04	0.04	0.00	0.18	0.00	0.00	92.04	94.13
ZK1908-333.2-1	Mt_3	0.04	0.36	0.01	0.59	0.16	0.22	0.08	0.00	0.34	0.00	0.03	92.73	94.57
ZK1908-576.5-1-1	Mt_3	0.00	0.71	0.06	1.08	0.40	0.07	0.00	0.00	0.20	0.00	0.00	90.54	93.07
ZK1908-587.1-3	Mt_3	0.01	0.81	0.07	0.64	0.40	0.05	0.04	0.00	0.31	0.00	0.01	92.23	94.55
ZK1908-587.1-4	Mt_3	0.01	0.80	0.07	0.49	0.45	0.12	0.02	0.00	0.26	0.00	0.03	92.62	94.87
ZK1908-610.5-1	Mt_3	0.00	0.67	0.04	0.55	0.32	0.07	0.04	0.00	0.35	0.00	0.00	92.90	94.93
ZK1908-610.5-2	Mt_3	0.00	0.70	0.06	0.75	0.33	0.14	0.04	0.00	0.29	0.02	0.00	92.23	94.55
Average		0.01	0.53	0.04	0.77	0.27	0.10	0.03	0.00	0.24	0.00	0.01	92.21	94.28
ZK3912-369.22-1	Mt_4	0.04	0.09	0.02	0.08	0.06	0.00	0.10	0.02	0.17	0.03	0.00	93.39	93.98
ZK3912-369.22-2-2	Mt_4	0.02	0.04	0.01	0.04	0.17	0.03	0.74	0.00	0.25	0.03	0.00	92.55	93.87
ZK3912-369.22-4	Mt_4	0.00	0.13	0.00	0.02	0.00	0.05	0.19	0.00	0.29	0.00	0.00	92.73	93.41
ZK3912-433.82-5	Mt_4	0.10	0.11	0.02	0.03	0.19	0.14	0.07	0.00	0.32	0.02	0.20	91.15	92.34
ZK3912-525.25-2-1	Mt_4	0.07	0.34	0.07	0.40	0.00	0.45	0.07	0.04	0.00	0.01	0.00	92.51	93.95
ZK3912-525.25-4	Mt_4	0.00	0.12	0.03	0.06	0.12	0.45	0.10	0.03	0.11	0.00	0.00	93.02	94.06
ZK3912-571.7-1-1	Mt_4	0.00	0.75	0.06	0.06	0.16	0.12	0.00	0.00	0.09	0.00	0.00	93.50	94.73
ZK3912-571.7-1-2	Mt_4	0.03	0.42	0.02	0.01	0.09	0.06	0.00	0.00	0.08	0.00	0.00	93.73	94.42
ZK3912-571.7-2-1	Mt_4	0.01	0.25	0.06	0.35	0.06	0.12	0.00	0.07	0.00	0.00	0.00	92.59	93.49
Average		0.03	0.25	0.03	0.12	0.09	0.16	0.14	0.02	0.15	0.01	0.02	92.80	93.81
ZK1908-257(2)-3	Mt_5	0.00	0.63	0.01	0.63	0.21	0.15	0.01	0.00	0.80	0.00	0.00	92.66	95.09
ZK1908-547.1-1	Mt_5	0.01	0.69	0.03	1.20	0.20	0.04	0.06	0.00	1.23	0.00	0.01	90.54	93.99
ZK1908-232.45-1-1	Mt_5	0.00	0.76	0.03	0.59	0.13	0.23	0.04	0.00	0.14	0.01	0.00	92.43	94.36
ZK1908-232.45-1-2	Mt_5	0.01	0.72	0.02	0.71	0.27	0.38	0.07	0.00	0.18	0.00	0.01	92.17	94.54
ZK1908-257(1)-1	Mt_5	0.01	0.36	0.04	0.93	0.17	0.07	0.14	0.00	0.16	0.01	0.03	92.21	94.11
ZK1908-257(2)-2	Mt_5	0.03	0.46	0.07	1.78	0.14	0.11	0.05	0.00	0.70	0.03	0.06	90.58	94.00
ZK1908-523.1-2	Mt_5	0.00	0.51	0.05	0.74	0.35	0.09	0.03	0.00	0.21	0.03	0.00	93.14	95.14
ZK1908-547.1-2	Mt_5	0.01	0.73	0.05	1.10	0.38	0.07	0.00	0.00	0.24	0.00	0.00	91.11	93.68

Table 2. *Cont.*

Sample	Type	Na_2O	Al_2O_3	MgO	SiO_2	TiO_2	MnO	Cr_2O_3	NiO	V_2O_5	K_2O	CaO	FeO	Total
ZK1908-570.4-1	Mt_5	0.01	0.73	0.03	0.81	0.32	0.13	0.00	0.00	0.32	0.00	0.00	92.52	94.86
ZK1908-570.4-2	Mt_5	0.00	0.80	0.08	1.14	0.42	0.01	0.06	0.00	0.31	0.08	0.01	92.02	94.93
ZK3912-512.2-1-1	Mt_5	0.00	0.82	0.29	0.69	0.85	0.16	0.02	0.00	0.41	0.00	0.00	92.11	95.35
ZK3912-605-2-1	Mt_5	0.00	0.51	0.26	0.55	0.34	0.09	0.00	0.03	0.25	0.00	0.00	91.60	93.63
Average		0.01	0.64	0.08	0.90	0.31	0.13	0.04	0.00	0.41	0.01	0.01	91.92	94.47

To avoid potential distortion of trace element data by sulfide or silicate inclusions, analytical spots were carefully selected based on backscattered electron (BSE) image examination prior to analysis, ensuring the exclusion of any points containing such inclusions. Magnetite LA-ICP-MS in situ analysis was completed in the Key Laboratory of Metallogeny and Mineral The laser ablation system used for analysis was the RESOlution S-155 model with a 193 nm excimer laser (Applied Spectra Inc., Sacramento, CA, USA), and the inductively coupled plasma mass spectrometer (ICP-MS) was the ElementXR model (Thermo Fisher, Waltham, MA, USA). During the laser ablation process, each piece of single-point analysis data collection included approximately 2 s of pre-ablation, 20 s of blank signal, and 40 s of sample signal. The laser energy density was 5 J/cm^2, the ablation spot diameter was 30 μm, and the frequency was 6 Hz. SRM 610 glass was used as the external standard, and we adopted SRM 612 as the monitoring standard [43]. During offline data processing, we used magnetite iron EPMA analysis results as the internal standard, and processed data with the software Iolite (version 4.0) [44].

5. Results

For the magnetite electron probe microanalysis data of the Duobuza deposit, see Table 2. Magnetite's main component is TFeO; its content ranges from 90.54% to 93.97%; and its minor components include MgO, Al_2O_3, SiO_2, CaO, TiO_2, V_2O_5, Cr_2O_3, and MnO. Among them, SiO_2 (0.01%~1.78%) content is highly variable, mostly distributed within 0.03%~1.18%, with an average value of 0.65%; Al_2O_3 content ranges from 0.04% to 1.31%, with a minority of samples reaching >1.00% and an average value of 0.57%; MgO content is low and relatively stable, ranging from 0.01% to 0.29% with an average value of 0.05%; V_2O_5 (0.08%~1.23%) is concentrated within 0.17%~0.47%, with a minority of samples reaching >1.00% and an average value of 0.31%; TiO_2 (0.06%~0.85%) is concentrated within 0.30%~0.66%, with an average value of 0.30%; and MnO content ranges from 0.01% to 0.45%, with an average value of 0.12%. Additionally, Na_2O, NiO, K_2O, and CaO contents in magnetite are all low, and partial samples are below detection limits.

For magnetite LA-ICP-MS in situ micro-area analysis data, see Table 3. Analytical results show that magnetite's main trace elements include Sc, Co, Ni, Zn, Ga, Mo, Na, Ge, and Cr; among them, Co (0.55~103.62 ppm)'s average value is 28.64 ppm; Zn (37.92~810.23 ppm) and Ni (4.36~983.07 ppm) contents are highly variable, with average values of 210.65 ppm and 126.72 ppm; Ga (18.68~163.96 ppm) content is relatively stable, with an average value of 64.04 ppm; Cr (8.49~2406.15 ppm) content is highly variable, with an average value of 316.53 ppm; Ge (0.59~27.22 ppm), Mo (0.09~1.27 ppm), and Sc (0.76~22.59 ppm) contents are low and relatively stable, with average values of 2.21 ppm, 0.54 ppm, and 7.22 ppm; Na (8.89~104.39 ppm)'s average value is 35.24 ppm; Sn, Ca, Se, Zr, As, Cd, Sb, Cs, Pr, and Nd contents are low, and partial samples are below detection limits. Overall, samples are characterized by high Ni, Zn, Cr, and Ga and low Co, Ge, Mo, Sc, and Sn.

Table 3. LA-ICP-MS data (ppm) for magnetite of different occurrences from the Duobuza porphyry Cu (-Au) deposit.

Sample	Type	Na	Mg	Al	Si	Sc	Ti	V	Cr	Mn	Co	Ni	Zn	Ga	Ge	Mo	Sn
ZK0308-467.6-1	Mt_1	26.00	213.49	3972.65	902.41	4.97	2577.21	1865.77	45.37	428.45	3.34	6.47	172.88	63.64	2.64	0.29	1.57
ZK0308-467.6-2	Mt_1	-	592.62	4702.06	746.60	5.83	2578.82	1661.32	72.43	1192.08	6.32	4.63	175.58	67.86	1.28	0.69	1.60
ZK0308-467.6-3	Mt_1	15.24	638.70	4837.26	936.44	8.94	4485.23	1633.07	80.51	1181.32	0.55	8.83	220.30	62.70	2.25	0.68	2.57
ZK0308-467.6-4	Mt_1	-	544.98	4503.98	814.47	5.38	2646.67	1600.55	72.98	718.29	4.01	4.36	166.74	65.63	1.51	0.60	1.37
ZK1908-215.5-1	Mt_1	-	231.29	2939.86	740.05	4.31	1420.56	1814.65	58.65	595.98	6.99	43.98	77.78	56.01	1.43	0.46	-
ZK1908-215.5-2	Mt_1	14.76	418.35	3876.11	781.33	3.86	6761.90	2166.83	72.33	654.09	9.81	49.23	95.48	61.53	1.62	0.55	2.40
ZK1908-215.5-4	Mt_1	-	373.24	3949.22	683.74	5.40	5089.66	2049.22	88.12	567.95	16.03	60.86	94.47	68.53	-	0.44	1.98
ZK1908-257-2-4-1	Mt_1	21.95	277.33	4452.94	1380.58	9.46	1334.74	3824.96	-	1241.61	42.69	62.61	516.40	75.46	-	0.43	1.32
ZK1908-350.3-3	Mt_1	31.08	486.68	4429.71	1103.29	6.87	1832.58	1998.89	92.11	686.87	19.66	57.99	100.76	70.23	1.59	1.25	-
ZK1908-456.4-1	Mt_1	-	151.89	3721.67	-	4.14	3217.13	4316.98	764.63	493.17	25.57	263.40	117.41	82.42	0.97	0.15	1.72
ZK1908-456.4-2	Mt_1	33.14	313.53	2922.92	932.41	3.22	4555.44	3915.12	2406.15	390.34	34.91	211.71	157.49	34.52	-	0.17	1.27
ZK1908-587.1-1	Mt_1	-	243.52	4093.80	693.31	13.99	2304.43	1561.89	2236.02	1000.28	27.36	94.11	537.91	49.19	0.93	0.41	1.09
ZK1908-587.1-2	Mt_1	17.78	2764.54	7717.92	-	3.77	1850.74	1509.75	1582.89	1388.62	15.05	130.52	589.98	59.57	-	0.12	-
ZK1908-635.9-2	Mt_1	14.49	421.62	3309.58	588.17	10.76	3239.54	2134.75	51.65	563.12	16.10	16.80	181.12	60.05	-	0.27	1.87
ZK3912-433.82-3	Mt_1	100.90	1226.14	7184.81	1086.89	19.19	3203.37	2394.77	83.91	853.37	18.15	42.09	341.48	68.98	27.22	0.51	2.15
Average		30.59	593.19	4440.97	876.13	7.34	3139.87	2296.57	550.55	797.04	16.44	70.51	236.38	63.09	4.14	0.47	1.74
ZK1908-222.7-1-2	Mt_2	13.21	384.87	3669.03	793.52	3.69	840.18	1063.52	61.76	1124.94	16.80	125.56	97.14	71.64	1.01	0.33	0.86
ZK1908-333.2-2	Mt_2	12.17	762.57	3716.69	281.39	10.10	1449.31	1590.37	75.71	983.34	33.11	91.56	119.49	76.67	1.45	0.68	0.87
ZK1908-350.3-1	Mt_2	-	343.22	3102.15	1019.26	3.86	1673.15	1671.89	18.10	424.17	14.79	66.55	78.45	58.75	0.87	0.21	1.25
ZK1908-350.3-2	Mt_2	-	426.51	3799.70	909.92	3.99	2952.81	1325.24	15.85	610.44	15.25	62.82	90.47	58.56	1.00	0.76	1.58
ZK1908-576.5-2-1	Mt_2	56.31	557.83	3936.18	1032.08	7.79	2076.08	1199.75	-	845.21	17.96	83.53	98.06	57.55	1.44	0.87	1.34
ZK1908-576.5-2-2	Mt_2	-	568.16	4249.96	710.68	5.55	2356.48	1290.05	35.69	861.07	23.46	83.75	123.90	66.47	2.13	0.66	1.16
ZK1908-576.5-2-3	Mt_2	-	709.53	3922.89	681.23	11.13	3592.24	2600.93	92.06	1548.58	36.90	98.72	152.56	81.09	1.30	0.59	2.91
ZK1908-610.5-3	Mt_2	-	543.26	4314.02	783.47	7.79	1825.78	2005.89	54.74	1072.95	28.68	63.29	248.47	63.01	1.28	0.40	-
ZK1908-635.9-1	Mt_2	19.74	715.45	4976.94	918.57	9.55	4923.07	1288.44	67.93	1100.35	10.25	24.37	167.04	76.32	1.30	0.46	2.96
ZK1908-654.9-1	Mt_2	15.07	440.43	4778.77	-	5.37	2083.93	1219.52	20.63	1267.10	12.63	25.77	123.17	66.22	1.37	0.32	1.23
ZK1908-654.9-2	Mt_2	14.09	740.75	4801.38	-	5.87	3616.25	1227.49	-	1099.74	22.82	24.86	137.42	71.06	1.63	0.25	3.03
ZK1908-654.9-3	Mt_2	-	585.67	4509.33	-	6.33	2125.61	1092.75	55.24	1123.29	27.41	27.68	162.44	67.07	1.50	0.52	1.19
ZK1908-584.15-1	Mt_2	25.60	123.14	2193.10	1078.62	3.35	1402.30	2086.36	1277.70	433.34	22.78	351.79	289.55	35.86	1.32	0.50	4.11
Average		22.31	530.88	3997.70	820.87	6.49	2378.25	1512.48	161.40	961.12	21.76	86.94	145.24	65.41	1.35	0.51	1.87
ZK1908-198.6-1	Mt_3	-	257.80	2850.22	1071.88	2.83	1072.45	1389.54	-	731.51	11.14	67.92	88.28	58.92	1.37	0.19	0.84
ZK1908-198.6-2	Mt_3	47.24	213.00	2544.89	1435.18	2.93	3907.81	1271.72	27.19	500.94	8.67	59.11	96.02	56.25	1.25	0.28	3.32
ZK1908-215.5-3	Mt_3	13.22	265.67	3069.95	831.50	2.36	1407.10	1833.58	52.69	658.59	13.91	46.56	99.87	56.55	2.68	-	-
ZK1908-257-1-2	Mt_3	-	176.37	3566.75	666.17	7.47	1402.52	806.90	9.34	1030.01	46.77	68.95	259.55	62.31	1.42	0.58	1.40
ZK1908-257-2-1	Mt_3	25.62	230.95	3153.26	882.68	10.80	3786.25	843.03	-	1223.30	55.71	50.76	232.07	53.31	1.01	0.88	2.25
ZK1908-257-2-3	Mt_3	-	145.82	3707.09	861.55	12.77	2585.53	4359.60	-	1201.29	44.58	52.25	406.27	83.42	1.82	0.85	1.13
ZK1908-323.9-1	Mt_3	26.76	79.20	2644.05	863.50	3.90	1317.40	1027.06	8.49	498.07	16.83	88.49	560.22	44.91	-	0.38	0.87

Table 3. *Cont.*

Sample	Type	Na	Mg	Al	Si	Sc	Ti	V	Cr	Mn	Co	Ni	Zn	Ga	Ge	Mo	Sn
ZK1908-333.2-1	Mt_3	8.89	469.63	3524.37	2010.92	3.20	1312.84	1858.20	29.49	2571.06	9.48	56.25	100.72	37.94	1.51	0.46	-
ZK1908-523.1-1	Mt_3	12.25	207.22	3197.37	1100.41	4.75	1425.77	1729.88	1356.95	349.44	27.66	187.18	280.29	42.14	-	0.39	-
ZK1908-587.1-3	Mt_3	18.50	561.85	4558.19	650.70	6.49	2956.62	1309.70	191.10	955.56	27.23	72.41	148.29	68.66	-	0.32	1.45
ZK4720-493.7-3-1	Mt_3	103.30	634.95	2759.23	4832.16	3.10	2415.76	1797.75	32.99	434.17	30.31	93.08	55.63	46.69	-	0.45	-
ZK4720-590.1-1	Mt_3	-	277.85	2744.75	943.00	3.90	1421.96	1511.46	25.11	483.29	40.58	115.88	87.44	49.90	0.59	0.58	1.33
ZK4720-590.1-2	Mt_3	93.14	703.79	3888.50	4983.60	6.97	2075.25	1383.13	-	628.13	39.99	137.06	84.55	60.82	1.26	0.52	1.11
ZK4720-590.1-4	Mt_3	29.24	495.53	3165.14	6544.43	5.31	1168.38	1813.20	248.06	840.41	91.70	99.70	87.61	53.94	1.28	0.19	-
Average		37.82	337.12	3240.98	1976.98	5.48	2018.26	1638.20	198.14	864.70	33.18	85.40	184.77	55.41	1.42	0.47	1.52
ZK1908-547.1-3	Mt_4	30.94	85.05	3333.39	1592.40	4.58	1502.94	1422.67	1169.32	528.96	21.33	153.93	249.01	42.97	-	0.29	1.00
ZK3912-433.82-5	Mt_4	50.89	57.51	942.22	414.48	2.25	1638.58	2205.21	19.37	1703.52	11.64	34.04	129.26	18.68	11.63	0.58	-
ZK3912-525.25-2-1	Mt_4	23.01	957.30	2931.70	2958.43	3.62	903.23	289.86	14.01	2625.44	7.33	208.40	60.03	58.46	2.34	0.54	2.09
ZK3912-525.25-4-1	Mt_4	-	91.87	995.83	1259.59	0.76	1637.26	566.89	551.17	2888.27	7.66	190.89	37.92	48.40	1.57	0.70	1.57
ZK3912-571.7-1	Mt_4	-	491.91	3264.66	807.38	4.35	1037.87	357.82	15.99	871.78	76.00	540.61	312.50	49.39	2.31	1.04	2.20
ZK3912-571.7-2	Mt_4	-	723.51	1302.48	3515.18	3.97	845.97	253.00	-	794.77	74.79	983.07	58.51	43.71	1.72	1.22	1.73
Average		34.95	401.19	2128.38	1757.91	3.25	1260.98	849.24	353.97	1568.79	33.12	351.82	141.21	43.60	3.92	0.73	1.72
ZK1908-232.45-1-1	Mt_5	17.30	126.95	2942.65	753.44	12.33	4398.94	1080.21	-	3492.71	36.59	147.18	810.23	140.11	1.72	0.93	2.86
ZK1908-232.45-1-2	Mt_5	17.44	167.06	3410.57	744.84	13.27	5025.89	1054.90	-	3796.12	34.59	158.10	484.04	163.96	1.54	1.17	3.45
ZK1908-257-1-1	Mt_5	28.51	189.25	2911.08	947.55	5.08	5368.01	1167.51	-	949.25	61.29	86.42	696.06	50.77	1.23	0.32	1.75
ZK1908-257-2-2	Mt_5	103.41	721.05	4149.87	9229.87	16.93	5540.21	3948.30	-	900.05	103.62	99.59	282.00	51.38	2.07	0.95	12.17
ZK1908-523.1-2	Mt_5	-	341.70	3230.87	901.89	13.49	2786.15	1165.53	96.11	857.47	47.49	136.98	185.11	53.01	0.94	0.50	1.63
ZK1908-547.1-2	Mt_5	17.48	531.72	4402.47	1473.53	7.98	2892.23	1532.30	64.62	524.04	37.26	178.55	110.68	94.39	1.74	0.09	1.97
ZK1908-570.4-1	Mt_5	-	626.15	3981.03	1085.52	7.32	2358.29	1798.90	96.92	733.52	26.29	61.43	107.37	78.48	1.13	0.11	1.56
ZK3912-510.8-2-1	Mt_5	-	55.44	3105.09	817.09	0.91	3082.77	296.62	743.02	2602.32	4.40	204.00	312.70	45.86	0.91	0.32	1.28
ZK3912-512.2-1	Mt_5	-	2128.34	3894.07	6690.72	10.03	3608.16	1859.05	-	1170.05	78.49	280.98	171.14	75.44	1.46	0.63	3.07
ZK3912-512.2-2	Mt_5	37.00	3405.85	4347.45	7906.21	21.30	4136.16	1907.07	-	1889.50	47.40	261.66	217.84	88.70	2.45	0.78	5.19
ZK3912-605-1	Mt_5	104.39	1979.86	5531.60	6860.70	22.59	4561.42	1106.43	-	836.57	46.96	189.75	491.41	72.06	1.94	1.27	2.14
ZK3912-605-2	Mt_5	11.64	1450.21	4188.75	3681.76	15.67	4828.36	1341.80	-	671.29	46.78	245.89	202.47	100.14	1.49	1.05	3.04
ZK4720-493.4-3	Mt_5	20.89	551.24	2927.76	5901.48	2.67	2927.88	2103.57	-	713.34	7.43	63.33	65.30	53.07	1.79	0.27	0.85
ZK4720-543.1-3-1	Mt_5	101.93	1050.92	3476.34	7947.53	7.40	3054.13	403.98	8.59	475.14	4.64	248.30	55.70	68.93	1.57	0.20	2.55
Average		46.00	951.84	3749.97	3924.44	11.21	3897.76	1483.30	201.85	1400.81	41.66	168.73	299.43	81.16	1.57	0.61	3.11

https://doi.org/10.3390/min16030288

6. Discussion

6.1. Genetic Types of Magnetite

Based on TiO_2, Al_2O_3, MnO, and MgO contents, magnetite can be classified into several types, including magmatic segregation Ti-magnetite, volcanic, contact metasomatic, skarn, sedimentary–metamorphic, and acidic–alkaline magmatic varieties [45,46]. Using Ni/Cr vs. Ti, Al + Mn vs. Ti + V, and Ti vs. V diagrams, magnetite can be further categorized into magmatic magnetite and hydrothermal magnetite [1,2,4,6].

Compared to hydrothermal magnetite, magmatic magnetite typically contains higher concentrations of Ti, V, Mn, Ni, Zn, and Ge, and lower Sn content [1,2,4–6]. Magmatic magnetite is notably richer in Ti compared to hydrothermal magnetite [1]. Magnetite associated with intermediate-acidic magmas exhibits lower Ni/Cr ratios, whereas most hydrothermal magnetite shows Ni/Cr ratios ≥ 1 [47]. In the Duobuza deposit, Mt_1 has Ni/Cr ratios ranging from 0.04 to 0.69, with samples predominantly falling within the magmatic magnetite field, indicating a magmatic origin. In contrast, Mt_2, Mt_3, Mt_4, and Mt_5 samples are mainly plotted in the hydrothermal magnetite field, indicating that they are hydrothermal magnetite (Figure 7).

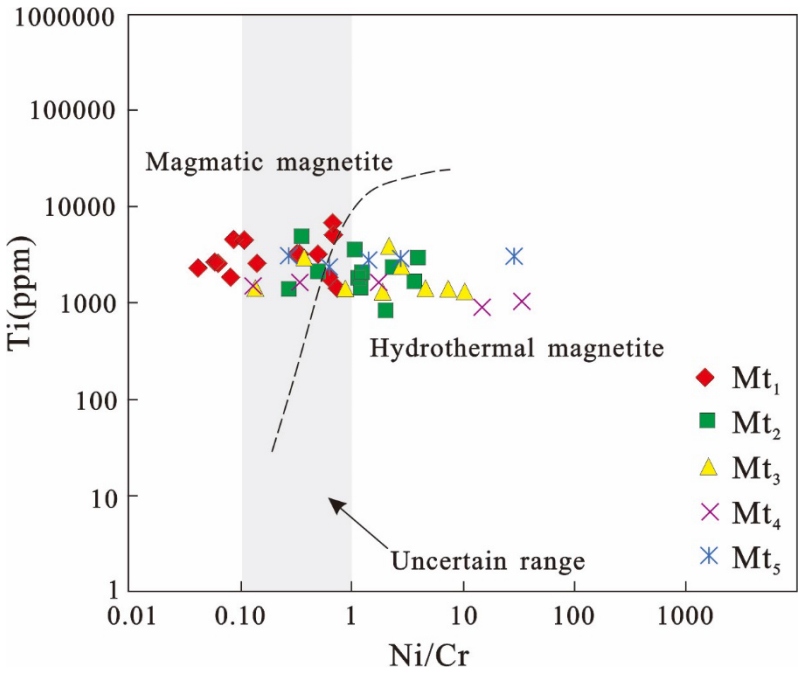


Figure 7. Ni/Cr vs. Ti discrimination diagram for magnetite (modified after [4,48]).

Magnetite from mafic–ultramafic rocks and related deposits typically contains approximately 0.5% to >10% TiO_2 and up to 0.78% V_2O_3. In intermediate-acidic rocks and related deposits, magnetite exhibits significantly lower TiO_2 content (~0.1%–0.8%) and extremely low V_2O_3 content [48]. Magnetite from Duobuza has TiO_2 content ranging from 0.06% to 0.95% and V_2O_3 content concentrated between 0.17% and 0.45% (Table 2), characterized by low Ti and low V. Its Mg (0.01%~0.29%) and Mn (0.01%~0.45%) contents are considerably lower than those in magnetite from ultramafic–mafic magmas, but similar to magnetite in intermediate-acidic rocks such as granite [48], indicating a genetic relationship with intermediate-acidic magmas.

6.2. Elemental Geochemical Characteristics

Elemental contents vary across different types of magnetite in the Duobuza deposit. Mt_1 is characterized by high Ti, V, Al, and Cr and low Mn and Si, with the highest V

(avg. 2296.57 ppm), Al (avg. 4440.97 ppm) and Cr (avg. 550.55 ppm) and the lowest Mn (avg. 797.04 ppm). Mt_2 shows high Ti and Al and low Si and Cr, with the lowest Si (avg. 820.87 ppm) and Cr (avg. 161.40 ppm). Mt_3 has high Al and low Mg, displaying the lowest Mg (avg. 337.12 ppm). Mt_4 features low Ti, Al, V, and Zn and high Mn, containing the lowest Al (avg. 2128.38 ppm), V (avg. 849.24 ppm), Ti (avg. 1260.98 ppm), and Zn (avg. 141.21 ppm) and the highest Mn (avg. 1568.79 ppm). Mt_5 possesses high Mg, Si, Ti, Al, Mn, and Zn and low Cr, showing the highest Mg (avg. 951.84 ppm), Ti (avg. 3897.76 ppm), Si (avg. 3924.44 ppm), and Zn (avg. 299.43 ppm), with a significantly narrower Si content range than other magnetite types (Table 3; Figures 8 and 9A).

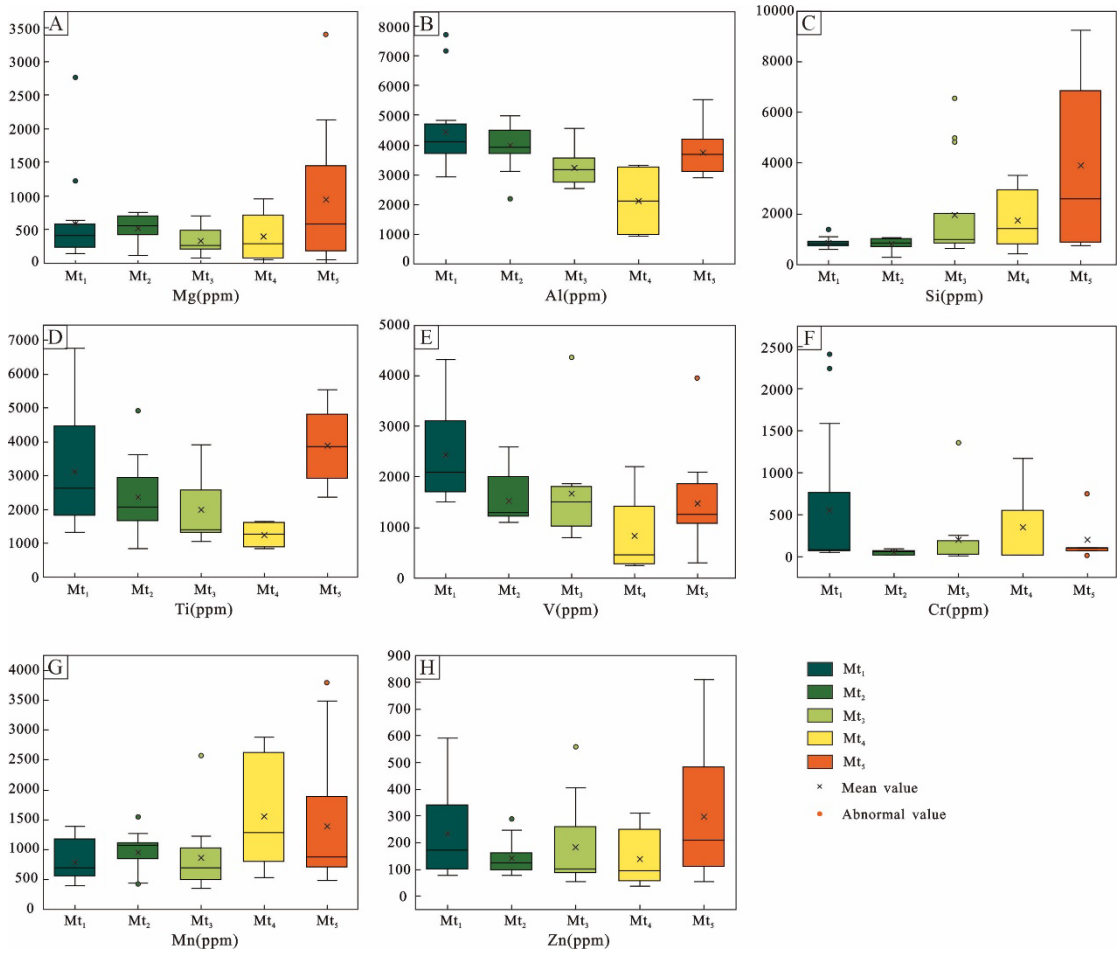


Figure 8. Comparative box plot showing Mg (**A**), Al (**B**), Si (**C**), Ti (**D**), V (**E**), Cr (**F**), Mn (**G**), and Zn (**H**) contents in magnetite.

Trace element correlations also differ among magnetite types in the Duobuza deposit. Mt_1 exhibits strong positive correlations between V and Ni and good positive correlations between Al and Mn, Mg and Sc, and Mn and Mg (Figure 9B,F–H). Mt_2 exhibits a prominent positive Mg-Sc correlation (Figure 9B). Mt_3 displays a marked positive Mg-Si correlation (Figure 9E). Mt_4 features strong positive Ge-V and Mg-Si correlations (Figure 9D), along with a significant negative Ni-V correlation (Figure 9H). Mt_5 shows weak positive Mg-Sc and Mg-Si correlations (Figure 9B). Mt_1 has a broad Ni content distribution range but a narrow Mn distribution range (Figure 9C,G,H). Mt_1, Mt_2, Mt_3, and Mt_4 exhibit similar Sc contents, whereas Mt_5 has significantly higher Sc than other types (Figure 9B). Additionally, Mt_4 exhibits a broad V distribution range (Figure 9H), and Mt_5 shows broad Si and V distribution ranges (Figure 9A,E,H).

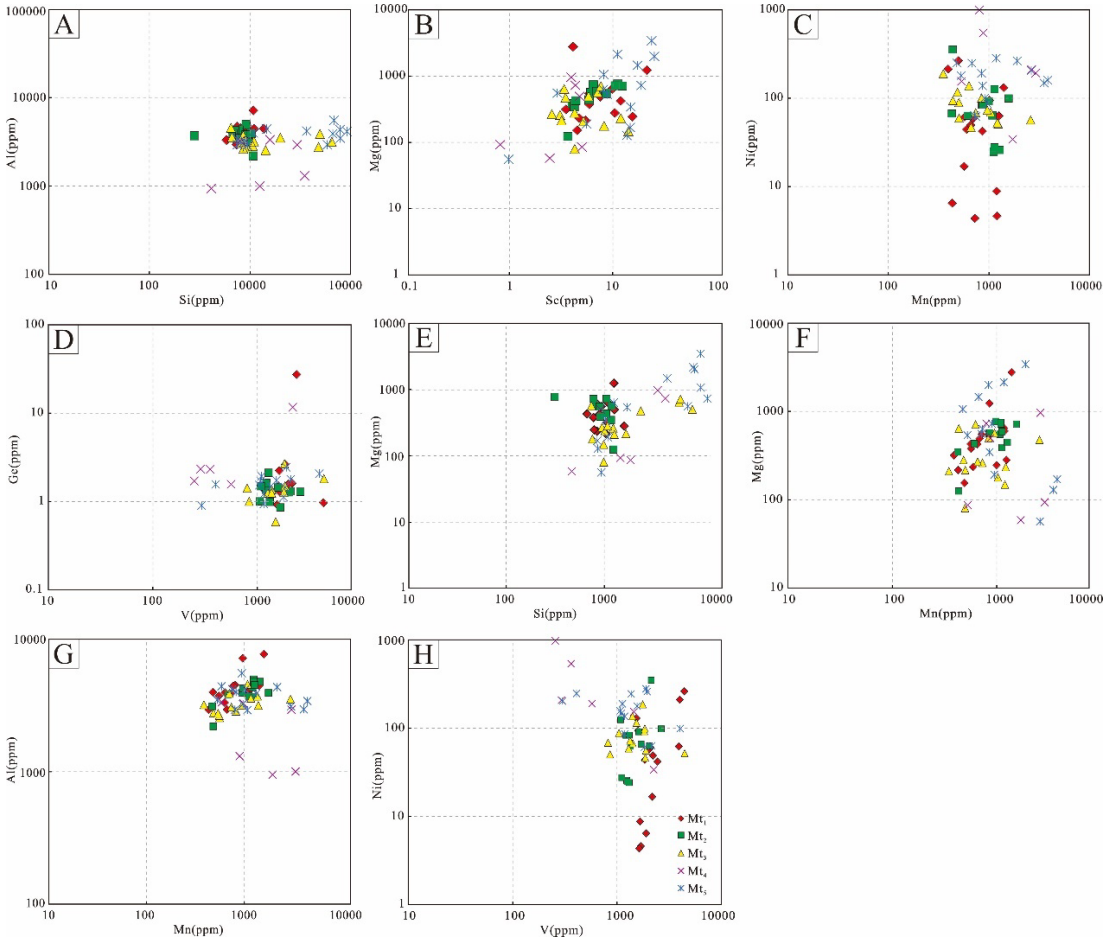


Figure 9. Binary diagrams for trace elements: (**A**) Al-Si; (**B**) Mg-Sc; (**C**) Ni-Mn; (**D**) Ge-V; (**E**) Mg-Si; (**F**) Mg-Mn; (**G**) Al-Mn; (**H**) Ni-V.

Elements in magnetite and other spinel-group minerals primarily occur in two forms: (1) as micron-scale mineral inclusions and (2) via isomorphism into the magnetite crystal lattice [49], which is characterized by negative correlations with FeO. Magnetite from the Duobuza porphyry Cu (-Au) deposit shows negative correlations between FeO and SiO_2/MgO (Figure 10), indicating that Si^{4+} and Mg^{2+} mainly enter the magnetite lattice by isomorphic substitution of Fe^{3+}.

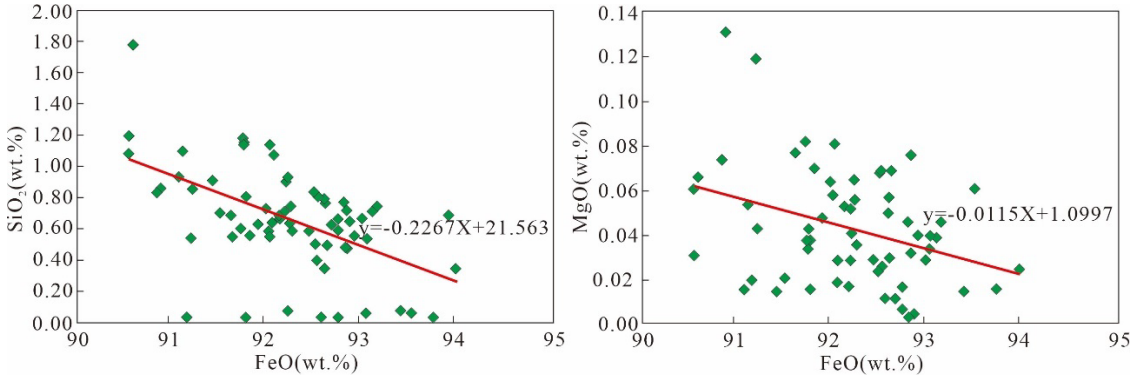


Figure 10. Whole-rock oxide variation diagrams of FeO vs. SiO_2 and FeO vs. MgO.

Correlations of V-Ni, Mn-Mg, and Al-Mn can serve as discriminators for magmatic magnetite (Mt_1) versus hydrothermal magnetite (Mt_2, Mt_3, Mt_4, Mt_5) in the Duobuza

deposit. High Mg, Si, Ti, Al, Mn, and Zn contents are diagnostic of ore-bearing magnetite (Mt_5), while the positive Mg-Sc correlation serves to distinguish Mt_1 from Mt_2.

6.3. Physicochemical Conditions of Magnetite Formation

Magnetite contains various trace elements, and its trace element composition varies due to influences from temperature, oxygen fugacity, fluid composition, host rocks, and coexisting minerals [1].

6.3.1. Temperature

(1) Formation Temperature of Magnetite

Temperature is a critical controlling factor in the formation of magnetite [50]. During magnetite crystallization, Ti typically substitutes for Fe^{3+} in the lattice, resulting in a positive correlation between formation temperature and Ti content [1,5,6]. Thus, Ti can be employed as a geothermometer for magnetite.

In the Duobuza deposit, average Ti contents are as follows: Mt_1 (3139 ppm), Mt_2 (2378 ppm), Mt_3 (2018 ppm), Mt_4 (1260 ppm), and Mt_5 (3897 ppm). Mt_4 has a narrow Ti distribution range and a significantly lower average Ti content compared to the other types, indicating the lowest and most stable formation temperature. Mt_5 exhibits the highest average Ti, reflecting the highest formation temperature. Temperatures decrease gradually from Mt_1 to Mt_4. Mt_5, associated with magnetite–quartz–chalcopyrite veins and closely linked to chalcopyrite, which is formed at higher temperatures than the other types, suggests high-temperature ore-forming fluids at the Duobuza deposit.

The Al + Mn-Ti + V diagram is an effective tool for constraining magnetite formation temperatures [1,51]. Most magnetite samples from the Duobuza deposit are plotted within the 300~500 °C and >500 °C fields on this diagram (Figure 11), indicating formation under moderate- to high-temperature hydrothermal conditions. Magnetite types Mt_3 and Mt_4 exhibit relatively lower formation temperatures compared to Mt_1, Mt_2, and Mt_3, with Mt_4 recording the lowest temperatures (Figure 11).

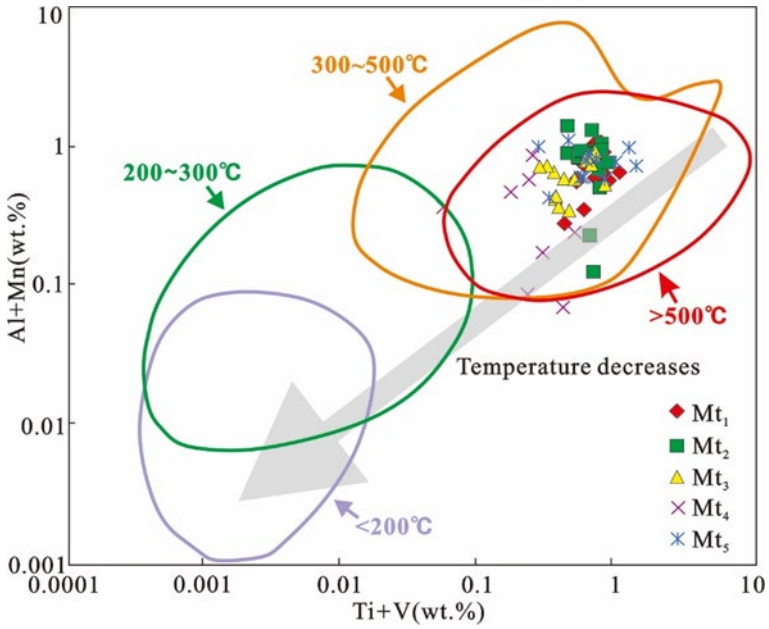


Figure 11. Al + Mn vs. -(Ti + V) discrimination diagram for magnetite (modified after [1]).

(2) Temperature Control of Element Distribution in Magnetite

Geochemical analysis of trace elements in magnetite from the Duobuza deposit reveals distinct genetic patterns based on correlations with Ti: for Mt_1, Mt_2, and Mt_3, elements such as Al, Ga, Mn, Mo, and Co exhibit no significant correlation with Ti (Figure 12A–E), indicating temperature-independent incorporation of these elements; conversely, elements like Sc, V, Zn, and Ni display non-linear variations with Ti (Figure 12F–I), suggesting that temperature partially controls their enrichment but is not the sole governing factor.

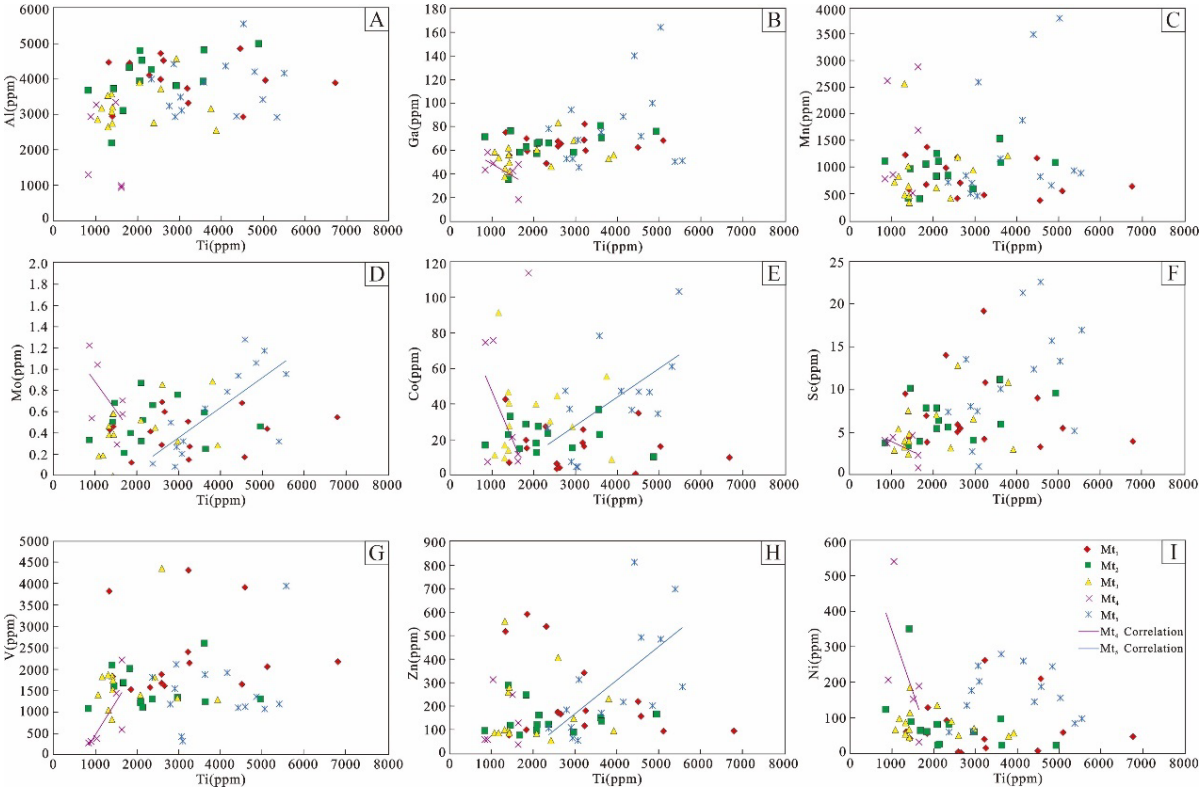


Figure 12. Correlation analysis of trace elements and Ti in different types of magnetite: (**A**) Al-Ti; (**B**) Ga-Ti; (**C**) Mn-Ti; (**D**) Mo-Ti; (**E**) Co-Ti; (**F**) Sc-Ti; (**G**) V-Ti; (**H**) Zn-Ti; (**I**) Ni-Ti.

In Mt_5, Mo shows a strong positive correlation with Ti (Figure 12D), while Co and Zn exhibit weak positive correlations (Figure 12E,H), implying a systematic increase in these elements with rising temperature. However, Ga, Mn, and Sc display no linear trends relative to Ti (Figure 12B,C,F), confirming that temperature is not the primary control for these constituents. For Mt_4, V shows a strong positive correlation with Ti (Figure 12G), reflecting thermal enrichment, whereas Ga, Mo, Co, Sc, and Ni display weak negative correlations (Figure 12B,D–F,I), indicating that their concentrations decrease at higher temperatures. Notably, Al, Mn, and Zn do not exhibit a linear relationship with Ti despite broad compositional ranges (Figure 12A,C,H), further reinforcing that temperature alone cannot explain their distribution patterns.

6.3.2. Oxygen Fugacity

Oxygen fugacity significantly influences the valence states of trace elements such as V, Sn and Mn in magnetite. For example, Sn^{4+} substitutes more readily for Fe^{3+} than Sn^{2+} in magnetite [52]. Unlike other monovalent elements (Si, Al, Ba, Ta) that increase with rising Ti, V in magnetite follows Ti trends at high Ti (>2500 ppm) but remains Ti-independent at low Ti (10~2500 ppm) [47]. V occurs as V^{3+}, V^{4+}, or V^{5+} in nature, primarily substituting for Fe^{3+} as V^{3+} in magnetite [51,52]. V content is co-controlled by temperature and oxygen

fugacity [47,50,53,54]. V behaves incompatibly under high oxygen fugacity [1,3,6,53], with its content inversely related to ore-forming oxygen fugacity: higher fugacity correlates with lower V [55].

Duobuza magnetite Mt_1 has the highest V content, with a progressive decrease in V from Mt_1 to Mt_4 (Figure 9E). Mt_4 exhibits a distinct positive correlation between V and Ti (Figure 12G), indicating that V is primarily temperature-controlled. The lower temperature of Mt_4 explains its relatively low V content (Figure 11). In contrast, Mt_1, Mt_2, Mt_3, and Mt_5 exhibit no significant V-Ti correlations (Figure 12G), suggesting that oxygen fugacity controls their V contents. High V in magmatic Mt_1 indicates low oxygen fugacity, whereas hydrothermal Mt_3 is formed under higher fugacity and Mt_4 under the highest. Early magmatic crystallization under low oxygen fugacity favors V incorporation into magnetite [51], suggesting that Mt_1 formed during early fractional crystallization. Hematite replacement along Mt_3 margins (Figure 6H,I) confirms high oxygen fugacity during its formation. Microphotographs show that Mt_5 is replaced by pyrite and chalcopyrite (Figure 6N,O). This magnetite type is closely associated with Cu mineralization within the deposit, and its formation under low oxygen fugacity facilitates the precipitation of sulfides.

6.4. Indicator of Deposit Types

Magnetite from different deposit types exhibits distinct trace element compositions influenced by ionic radius, valence states, magma/fluid temperature, and oxygen fugacity [47,56]. The Ti + V vs. Ca + Al + Mn and Ti + V vs. Al + Mn diagrams are effective tools for discriminating deposit types [2,3]. In the Ti + V vs. Ca + Al + Mn diagram, Duobuza magnetite is predominantly plotted within the porphyry deposit field (Figure 13A). In the Ti + V vs. Al + Mn diagram, it clusters in the porphyry and skarn + porphyry deposit fields (Figure 13B), with most Mt_2 samples falling in the skarn field, likely due to high Mn and Al contents [1,51]. These results align with the classification of Duobuza as a porphyry deposit, demonstrating that magnetite trace elements are effective indicators of deposit type.

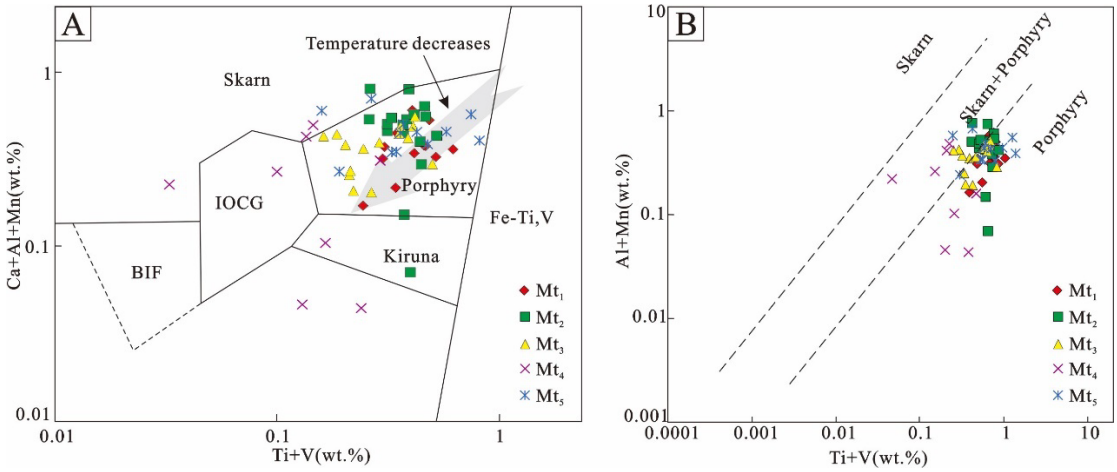


Figure 13. Discrimination diagrams for magnetite: (**A**) Ti + V vs. Ca + Al + Mn (modified after [3]); (**B**) Ti + V vs. Al + Mn (modified after [2]).

Comparison of trace elements between Duobuza magnetite and typical magmatic/hydrothermal deposits reveals similar distribution patterns to established trends (Figure 14A,B) [4]. Both magmatic and hydrothermal magnetite at Duobuza are enriched in Ga, Zn and V but depleted in Al, Co and Mg. Hydrothermal magnetite shows greater depletion in Cr and V compared to magmatic types (Figure 14A,B). Elements such as V, which have high abundances in magmas and ionic radii/charges similar to Fe, exhibit high partition coefficients, favoring isomorphic substitution into magnetite during crystalliza-

tion [3]. Incompatible elements (e.g., Al and Mg) are excluded from the lattice, leading to their depletion. Hydrothermal magnetite trace element patterns at Duobuza match those of porphyry deposits (Figure 14B), confirming their use as discriminators of deposit type.

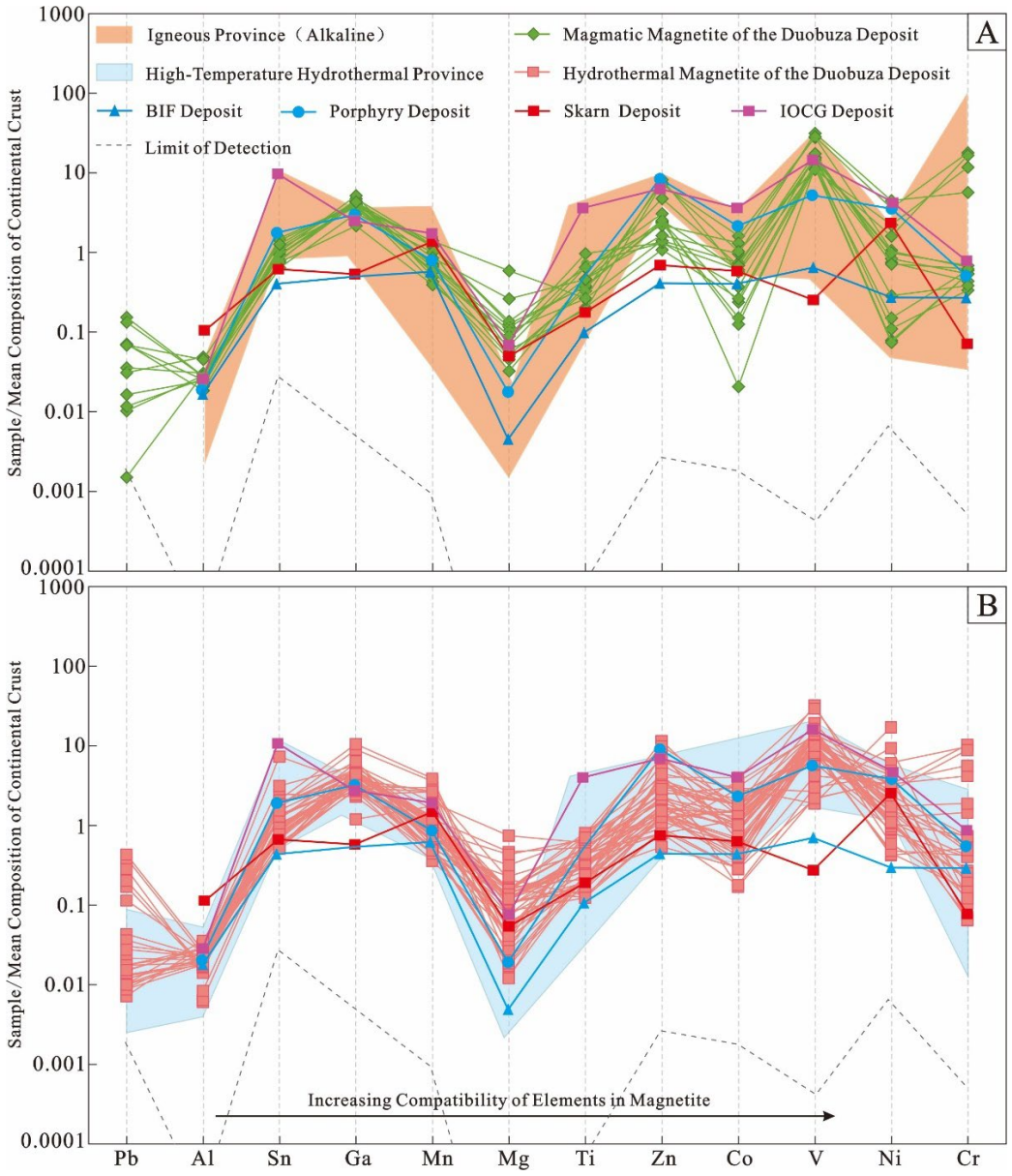


Figure 14. Primitive mantle-normalized (spider) diagram for trace elements in magnetite [4,57]: (**A**) Magmatic Magnetite of Duobuza deposit; (**B**) Hydrothermal Magnetite of Duobuza deposit.

6.5. Implications for Deposit Genesis

Within the Duolong ore district, abundant magnetite is developed in the Duobuza, Bolong, and Naruo ore fields. To compare the chemical characteristics of magnetite within the district, electron probe microanalysis (EPMA) was conducted on selected magnetite samples from the Bolong deposit, and EPMA data for magnetite from the Naruo deposit were compiled (Table 4).

Table 4. Electron probe microanalysis (EPMA) data (%) of magnetite from the Bolong and Naruo porphyry Cu-Au deposits.

Deposit	Sample	Type	MgO	$A1_2O_3$	SiO_2	CaO	TiO_2	V_2O_5	Cr_2O_3	MnO	NiO	Data Source
Bolong	ZK17901-389.85-4	Magmatic magnetite	0.00	0.30	0.04	0.00	0.63	0.13	0.01	0.02	0.03	Unpublished data
	ZK17901-428.4-1		0.03	0.38	0.01	0.00	0.41	0.12	0.02	0.04	0.09	
	ZK17901-417.6-3-1		0.18	0.65	0.85	0.00	0.51	0.39	0.03	0.07	0.07	
	ZK17901-417.8-1		0.00	0.25	0.03	0.00	0.59	0.21	0.08	0.10	0.00	
	ZK17901-419.67-1	Hydrothermal magnetite	0.02	0.14	0.08	0.00	0.00	0.23	0.08	0.16	0.23	
	ZK17901-419.67-2		0.01	0.17	0.01	0.00	0.16	0.17	0.06	0.09	0.00	
	ZK17901-419.67-3		0.03	0.16	0.01	0.00	0.28	0.23	0.01	0.03	0.00	
	ZK17901-419.67-4		0.04	0.16	0.00	0.00	0.19	0.22	0.05	0.08	0.07	
	ZK17901-419.67-5-2		0.04	0.10	0.00	0.00	0.00	0.20	0.12	0.00	0.00	
	ZK17901-419.67-6		0.04	0.21	0.12	0.00	0.00	0.19	0.09	0.09	0.12	
	ZK17901-402.5-2		0.47	0.87	1.65	0.22	0.00	0.14	0.05	0.05	0.14	
	ZK17901-402.5-1		0.01	0.14	0.05	0.00	0.11	0.18	0.29	0.05	0.08	
	ZK17901-234.5-1		0.02	0.61	0.09	0.00	0.10	0.17	0.03	0.02	0.13	
	ZK17901-234.5-2		0.02	0.64	0.15	0.00	0.13	0.13	0.00	0.07	0.00	
	ZK17901-325.4-1		0.01	0.18	0.02	0.00	0.00	0.31	0.33	0.11	0.04	
	ZK17901-430.16-1-2		0.00	0.08	0.05	0.00	0.06	0.21	0.20	0.04	0.00	
	ZK17901-430.16-4		0.00	0.21	0.03	0.00	0.33	0.16	0.09	0.03	0.06	
	ZK17901-388.2-1-1		0.04	0.30	0.03	0.00	0.05	0.20	0.02	0.07	0.11	
	ZK17901-388.2-1-2		0.03	0.31	0.06	0.00	0.02	0.20	0.08	0.11	0.13	
	ZK17901-388.2-3		0.04	0.25	0.03	0.00	0.17	0.16	0.03	0.08	0.05	
	ZK17901-380.2-1		0.01	0.28	0.01	0.00	0.08	0.15	0.08	0.09	0.03	
	ZK17901-380.2-2		0.44	0.84	0.81	0.00	0.11	0.25	0.00	0.04	0.05	
	ZK17901-324.4-1		0.00	0.08	0.00	0.00	0.07	0.25	0.01	0.06	0.00	
	ZK17901-324.4-2		0.00	0.08	0.05	0.00	0.06	0.50	0.20	0.04	0.00	
Naruo	N-12	Magmatic magnetite	0.00	0.63	0.23	0.03	0.72	0.19	0.07	0.01	0.02	[58]
	N-ll		0.03	0.79	0.07	0.02	0.36	0.36	0.05	0.12	0.01	
	N-l		0.00	0.63	0.23	0.03	0.72	0.19	0.07	0.01	0.02	
	N-2	Hydrothermal magnetite	0.02	0.06	0.03	0.14	0.18	0.43	0.04	0.01	0.00	
	N-3		0.00	0.08	0.15	0.02	0.11	0.38	0.03	0.03	0.01	
	N-4		0.13	0.30	0.95	0.53	0.22	0.19	0.19	0.01	0.02	
	N-5		0.04	0.62	0.02	0.03	0.27	0.36	0.03	0.13	0.00	
	N-6		0.00	0.04	0.01	0.01	0.04	0.33	0.03	0.03	0.00	
	N-7		0.05	0.70	0.06	0.04	0.29	0.37	0.05	0.12	0.03	
	N-8		0.00	0.11	0.18	0.05	0.10	0.34	0.00	0.01	0.02	
	N-9		0.00	0.53	0.05	0.01	0.16	0.39	0.03	0.08	0.00	
	N-10		0.00	0.05	0.08	0.04	0.02	0.30	0.04	0.05	0.02	

Patrick Nadoll conducted experiments on over 1000 magnetite samples from diverse mineralization settings worldwide and systematically summarized their findings [1]. He discovered that magnetite exhibits significant and systematic variations in the contents of elements such as Mg, Al, Ti, V, Co, Ni, Zn, Cr, Mn, Ga, and Sn across different deposit types. Consequently, these trace elements can serve as discriminators for deposit type identification. Variations in analytical techniques and experimental conditions can lead to changes in detection limits. To obtain more accurate analytical results, it is essential to pre-process the upper limit values for the same element analysis results and to select representative sample data. Plotting this data collectively on a multi-element spider diagram can clearly visualize the variations in trace element concentrations within the magnetite. A comparative analysis of magmatic versus hydrothermal magnetite from the Duobuza, Bolong, and Naruo deposits within the Duolong ore district reveals distinct geochemical disparities.

Both magmatic and hydrothermal magnetite from the Duobuza deposit are depleted in Ni and Ca but enriched in V, Al, and Si. Magmatic magnetite from the Naruo deposit is depleted in Ni and Ca but enriched in Al and Ti, while its hydrothermal magnetite is depleted in Ni but enriched in Al and Si. Magmatic magnetite from the Bolong deposit is depleted in Ca but enriched in Al and Si, whereas its hydrothermal magnetite is depleted in Ca and Mn but enriched in Al and Si (Figure 15). Magnetite from all deposits in the Duolong ore district exhibits the common characteristic of being enriched in Si and Al but depleted

in Ca and Ni. This geochemical signature likely reflects shared source properties or similar magmatic–hydrothermal evolutionary pathways within the ore cluster. The similar elemental distribution patterns of magmatic magnetite from the Naruo and Duobuza deposits (Figure 15) suggest that their parental magmas had comparable chemical compositions and underwent similar fractional crystallization processes. Compared with magnetite from the Bolong and Naruo deposits, hydrothermal magnetite from Duobuza shows significantly higher Ti and V contents, indicating that the Duobuza hydrothermal system experienced higher temperatures and lower oxygen fugacity than those at Naruo and Bolong. Ti content in hydrothermal magnetite generally increases with rising temperature, while V^{3+} is more readily incorporated into the magnetite lattice under low-oxygen-fugacity conditions. This combination of high Ti and high V suggests that the Duobuza hydrothermal system formed at a relatively greater depth under higher temperatures and lower oxygen fugacity, which favored the enrichment of vanadium.

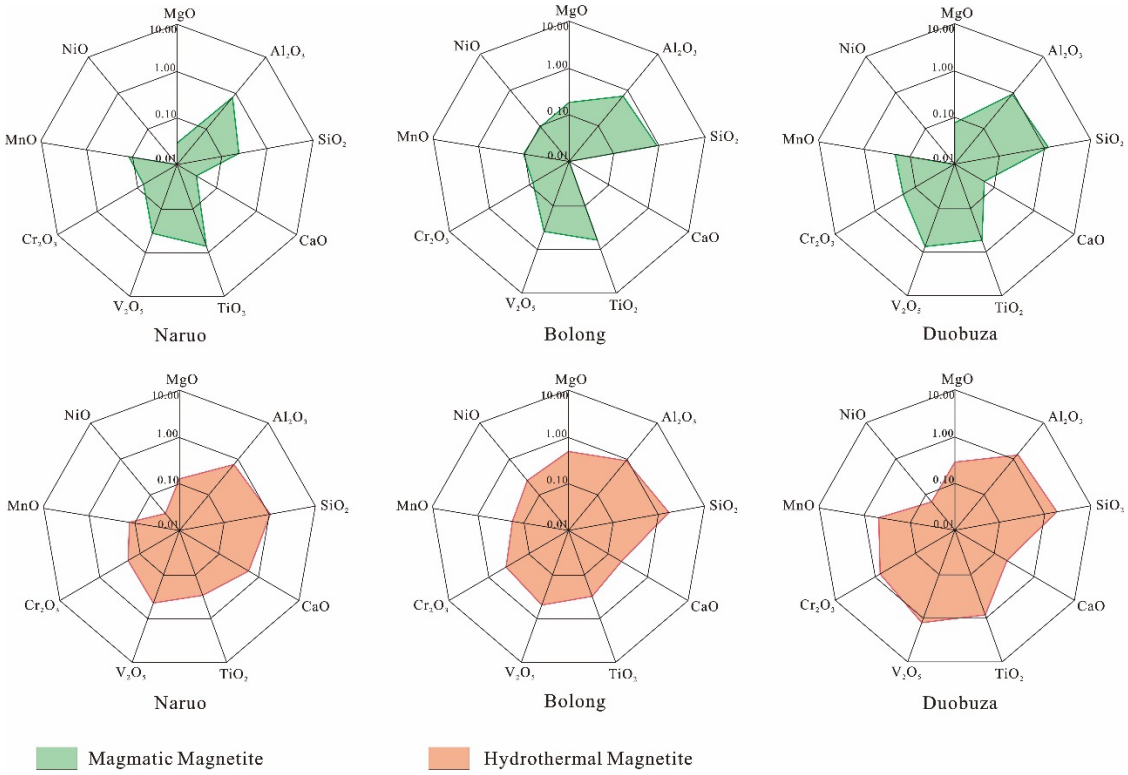


Figure 15. Multi-element radar diagrams comparing the geochemical signatures of the Naruo, Bolong, and Duobuza deposits.

7. Conclusions

This study, through integrated mineralogical and geochemical analyses, systematically clarifies the genetic types of magnetite and their formation environments in the Duobuza porphyry Cu–Au deposit. The main findings are as follows:

(1) Five distinct magnetite types with different occurrences and compositions are identified: magmatic magnetite Mt_1 (disseminated in granodiorite porphyry) and hydrothermal magnetites Mt_2–Mt_5. Each magnetite type exhibits unique trace element characteristics: Mt_1 is enriched in Ti, V, Al, and Cr but depleted in Mn and Si; Mt_2 is enriched in Ti and Al but depleted in Si and Cr; Mt_3 is enriched in Al and depleted in Mg; Mt_4 is characterized by low Ti, Al, V, and Zn but high Mn; and Mt_5 is enriched in Mg, Si, Ti, Al, Mn, and Zn but depleted in Cr. Among these, correlations of V with Ni and Mn and Mg and Al with Mn can serve as effective geochemical indicators to distinguish magmatic magnetite from hydrothermal magnetite in the Duobuza area.

(2) Magnetite from Duolong ore district formed in a medium- to high-temperature environment, with Mt_4 showing the lowest formation temperature. Magmatic magnetite Mt_1 formed under relatively low-oxygen-fugacity conditions, whereas hydrothermal magnetite Mt_4 formed under the highest oxygen fugacity conditions. Mt_5, which is closely associated with Cu mineralization, exhibits significantly elevated V content, reflecting its formation under low-oxygen-fugacity conditions that are conducive to the precipitation of metal sulfides.

(3) Trace element compositions of magnetite are effective tools for indicating deposit types. Regional comparisons show that magnetite from the Duobuza, Bolong, and Naruo deposits all share the characteristics of being enriched in Si and Al but depleted in Ca and Ni. The magmatic magnetite from Duobuza and Naruo exhibits similar elemental partitioning patterns, suggesting a genetic affinity between their source magmas. However, hydrothermal magnetite from Duobuza shows significantly higher Ti and V contents compared to those from Bolong and Naruo, indicating that its hydrothermal system was characterized by higher temperatures and lower oxygen fugacity.

Author Contributions: Conceptualization, X.F. and Q.W.; Methodology, X.F., Q.W. and S.L.; Validation, X.F., R.Z., Q.Z. and X.L.; Formal analysis, X.F., and C.G.; Investigation, X.F., Y.D. and S.L.; Resources, Q.W. and Y.D.; Original draft writing, X.F.; Review and editing, X.F., H.X. and X.L.; Project administration, X.F. All authors have read and agreed to the published version of the manuscript.

Funding: This study was financially supported by the National Deep Earth Exploration Science and Technology Major Project of the Ministry of Natural Resources, PRC (grant no. 2025ZD1006201); the National Natural Science Foundation of China (grant no. 42472140 and 42230813); Central Government Guided Local Scientific and Technological Development Funding Project (grant no. XZ202401YD0006); and the China Geological Survey Project (grant no. DD20230362 and DD20230054).

Data Availability Statement: The data are contained within this article.

Acknowledgments: We would like to express our sincere gratitude to Tibet Jinlong Co., Ltd. for their strong support, to the relevant personnel of the Fifth Geological Team of the Tibet Autonomous Region Geological and Mineral Exploration and Development Bureau for their assistance, and to the peer reviewers and editorial board members for their constructive comments and suggestions.

Conflicts of Interest: Author She Li is employed by Chinalco Tibet Jinlong Mining Co., Ltd. The paper reflects the views of the scientists and not the company.

References

1. Nadoll, P.; Angerer, T.; Mauk, J.L.; French, D.; Walshe, J. The chemistry of hydrothermal magnetite: A review. *Ore Geol. Rev.* **2014**, *61*, 1–32. [CrossRef]
2. Nadoll, P.; Mauk, J.L.; Leveille, R.A.; Koening, A.E. Geochemistry of magnetite from porphyry Cu and skarn deposits in the southwestern united states. *Miner. Depos.* **2015**, *50*, 493–515. [CrossRef]
3. Dupuis, C.; Beaudoin, G. Discriminant diagrams for iron oxide trace element fingerprinting of mineral deposit types. *Miner. Depos.* **2011**, *46*, 319–335. [CrossRef]
4. Dare, S.A.S.; Barnes, S.J.; Beaudoin, G.; Meric, J.; Boutroy, E.; Potvin-Doucet, C. Trace elements in magnetite as petrogenetic indicators. *Miner. Depos.* **2014**, *49*, 785–796. [CrossRef]
5. Dare, S.A.S.; Barnes, S.J.; Beaudoin, G. Variation in trace element content of magnetite crystallized from a fractionating sulfide liquid, Sudbury, Canada: Implications for provenance discrimination. *Geochim. Cosmochim. Acta* **2012**, *88*, 27–50. [CrossRef]
6. Knipping, J.L.; Bilenker, L.D.; Simon, A.C.; Reich, M.; Barra, F.; Deditius, A.P.; Walle, M.; Heinrich, C.A.; Holtz, F.; Munizaga, R. Trace elements in magnetite from massive iron oxide-apatite deposits indicate a combined formation by igneous and magmatic-hydrothermal processes. *Geochim. Cosmochim. Acta* **2015**, *171*, 15–38. [CrossRef]
7. Huang, X.W.; Sappin, A.A.; Boutroy, É.; Beaudoin, G.; Makvandi, S. Trace element composition of igneous and hydrothermal magnetite from porphyry deposits: Relationship to deposit subtypes and magmatic affinity. *Econ. Geol.* **2019**, *114*, 917–952. [CrossRef]

8. Sun, K.; Chen, B.; Deng, J. Biotite in highly evolved granites from the Shimensi W-Cu-Mo polymetallic ore deposit, China: Insights into magma source and evolution. *Lithos* **2019**, *350–351*, 105245. [CrossRef]
9. Lindsley, D.H. *Some Experiments Pertaining to the Magnetite-Ul-Vospinel Miscibility Gap*; American Mineralogist: Chantilly, VA, USA, 1981.
10. Li, G.M.; Li, J.X.; Qin, K.Z.; Zhang, T.P.; Xiao, B. Preliminary study on alteration and mineralization features and high-oxidated ore-forming fluids at Duobuza super-large Au-rich porphyry Cu deposit, western Tibet. *Miner. Depos.* **2006**, *25*, 411–414. (In Chinese)
11. Li, G.M.; Li, J.X.; Qin, K.Z.; Zhang, T.P.; Xiao, B. High temperature, salinity and strong oxidation ore-forming fluid at Duobuza gold-rich porphyry copper deposit in the Bangonghu tectonic belt, Tibet: Evidence from fluid inclusions. *Acta Petrol. Sin.* **2007**, *23*, 935–952. (In Chinese)
12. Li, J.X.; Li, G.M.; Qin, K.Z.; Xiao, B. Geochemistry of porphyries and volcanic rocks and ore-forming geochronology of Duobuza gold-rich porphyry copper deposit in Bangonghu belt, Tibet: Constraints on metallogenic tectonic settings. *Acta Petrol. Sin.* **2008**, *24*, 531–543. (In Chinese)
13. Zhang, Z.; Chen, Y.C.; Tang, J.X.; Li, Y.B.; Gao, K.; Wang, Q.; Li, Z.; Li, J.L. Alteration and vein systems of Duobuza gold-rich porphyry copper deposit, Tibet. *Miner. Depos.* **2014**, *33*, 1268–1286. (In Chinese)
14. Li, Y.B.; Duo, J.; Zhong, W.T.; Li, Y.C.; Qiang, B.W.D.; Chen, H.Q.; Liu, H.F.; Zhang, J.S.; Zhang, T.P.; Xu, Z.Z.; et al. An exploration model of the Duobuza porphyry Cu—Au deposit in Gaize Country, northern Tibet. *Geol. Explor.* **2012**, *48*, 274–287. (In Chinese)
15. Jiang, S.Q.; Sun, X.G.; Yang, T.Z.; Li, L.; Yin, X.B.; Wang, C.; Pan, Y.B. Integrated anomaly model and metallogenic prediction of the Duolong porphyry copper-gold ore concentration area in northern Tibet. *Geol. China* **2014**, *41*, 497–509. (In Chinese)
16. Li, J.X.; Qin, K.Z.; Li, G.M.; Evans, N.J.; Huang, F.; Zhao, J.X. Iron isotope fractionation during magmatic-hydrothermal evolution: A case study from the Duolong porphyry Cu-Au deposit, Tibet. *Geochim. Cosmochim. Acta* **2018**, *238*, 1–15. [CrossRef]
17. Lin, B.; Chen, Y.C.; Tang, J.X.; Wang, Q.; Song, Y.; Yang, C.; Wang, W.L.; He, W.; Zhang, L.J. $^{40}Ar/^{39}Ar$ and Rb-Sr ages of the Tiegelongnan porphyry Cu-(Au) deposit in the Bangong Co-Nujiang metallogenic belt of Tibet, China: Implication for generation of super-large deposit. *Acta Geol. Sin.* **2017**, *91*, 602–616. [CrossRef]
18. Hou, Z.Q.; Cook, N.J. Metallogenesis of the Tibetan collisional orogen: A review and introduction to the special issue. *Ore Geol. Rev.* **2009**, *36*, 2–24. [CrossRef]
19. Liu, Z.B.; Wang, W.L.; Song, Y.; Wang, Q. Geo-information Extraction and Integration of Ore-controlling Structure in the Duolong Ore Concentration Area of Tibet. *Acta Geosci. Sin.* **2017**, *38*, 803–812. (In Chinese)
20. Yang, C.; Beaudoin, G.; Tang, J.X.; Song, Y.; Wang, L.Q.; Huang, X.W. Hydrothermal fluid evolution at the Tiegelongnan porphyry-epithermal Cu (Au) deposit, Tibet, China: Constraints from H and O stable isotope and in-situ S isotope. *Ore Geol. Rev.* **2020**, *125*, 103694. [CrossRef]
21. Yang, C.; Beaudoin, G.; Tang, J.X.; Song, Y.; Wang, L.Q.; Huang, X.W. Cu-sulfide mineralogy, texture, and geochemistry in the Tiegelongnan porphyry-epithermal copper system, Tibet, China. *Miner. Depos.* **2022**, *57*, 759–779. [CrossRef]
22. Song, Y.; Tang, J.X.; Liu, Z.B.; Li, F.Q.; Wang, Q.; Xiao, Y.; Wang, Y.L. Mechanism of Tiegelongnan-Duobuza ramp style ore-controlling structure, Tibet: Evidence from geophysical exploration. *Miner. Depos.* **2019**, *38*, 1263–1277. (In Chinese)
23. Yang, H.H.; Song, Y.; Tang, J.X.; Wang, Q.; Gao, K.; Wei, S.G. Low temperature history of the Tiegelongnan porphyry–epithermal Cu (Au) deposit in the Duolong ore district of northwest Tibet, China. *Resour. Geol.* **2020**, *70*, 111–124. [CrossRef]
24. Tang, J.X.; Song, Y.; Wang, Q.; Lin, B.; Yang, C.; Guo, N.; Fang, X.; Yang, H.H.; Wang, Y.Y.; Gao, K.; et al. Geological Characteristics and Exploration Model of the Tiegelongnan Cu (Au-Ag) Deposit: The First Ten Million Tons Metal Resources of a Porphyry-epithermal Deposit in Tibet. *Acta Geosci. Sin.* **2016**, *37*, 663–690. (In Chinese)
25. Yang, C.; Beaudoin, G.; Song, Y.; Tang, J.X.; Wang, Y.Y.; Buret, Y.; Huang, X.W.; Lang, X.H.; Lin, B. Geochemistry of hydrothermal and stream sedimentary rutile in the Tiegelongnan porphyry-epithermal Cu (Au) deposit, Tibet: A tool for exploration. *Ore Geol. Rev.* **2024**, *167*, 105970. [CrossRef]
26. Ding, S.; Tang, J.X.; Zheng, W.B.; Zhang, Z.; Wang, Y.Y.; Lin, B. Zircon U-Pb Age and Geochemical Characteristics of Ore-Bearing Porphyry in the Naruo Copper (Gold) Deposit, Tibet. *Miner. Depos.* **2014**, *33*, 3–4. (In Chinese)
27. Li, J.X.; Qin, K.Z.; Li, G.M.; Evans, N.J.; Zhao, J.X.; Cao, M.J.; Huang, F. The Nadun Cu-Au mineralization, central Tibet: Root of a high sulfidation epithermal deposit. *Ore Geol. Rev.* **2016**, *78*, 371–387. [CrossRef]
28. Zhang, Z.; Fang, X.; Tang, J.X.; Wang, Q.; Yang, C.; Wang, Y.Y.; Ding, S.; Yang, H.H. Chronology, geochemical characteristics of the Gaerqin porphyry copper deposit in the Duolong ore concentration area in Tibet and discussion about the identification of the lithoscaps and the possible epithermal deposit. *Acta Petrol. Sin.* **2017**, *33*, 476–494. (In Chinese)
29. Lin, B.; Chen, Y.C.; Tang, J.X.; Song, Y.; Wang, Q.; Feng, J.; Li, Y.B.; Tang, X.Q.; Lin, X.; Liu, Z.B.; et al. Zircon U-Pb Ages and Hf Isotopic Composition of the Ore-bearing Porphyry in Dibao Cu(Au) Deposit, Duolong Ore Concentration Area, Xizang (Tibet), and Its Geological Significance. *Geol. Rev.* **2016**, *62*, 1565–1578. (In Chinese)

30. Lin, B.; Tang, J.X.; Chen, Y.C.; Song, Y.; Hall, G.; Wang, Q.; Yang, C.; Fang, X.; Duan, J.L.; Yang, H.H.; et al. Geochronology and genesis of the Tiegelongnan porphyry Cu(Au) deposit in Tibet: Evidence from U–Pb, Re–Os dating and Hf, S, and H–O isotopes. *Resour. Geol.* **2017**, *67*, 1–21. [CrossRef]
31. Wang, Q.; Tang, J.X.; Chen, Y.C.; Hou, J.F.; Li, Y.B. The metallogenic model and prospecting direction for the Duolong super large copper (gold) district, Tibet. *Acta Petrol. Sin.* **2019**, *35*, 879–896. (In Chinese) [CrossRef]
32. Tang, J.X.; Yang, H.H.; Li, H.W.; Wang, Q.; Li, Y.B.; Li, S.; Lin, B.; Li, F.Q.; Zhai, J.J.; Tang, X.Q.; et al. Geological characteristics and prospecting potential analysis of Duolong porphyry-epithermal copper (gold) ore district in Tibet. *China Min. Mag.* **2024**, *33*, 1–13. (In Chinese)
33. Duan, J.L.; Tang, J.X.; Li, Y.B.; Liu, S.A.; Wang, Q.; Yang, C.; Wang, Y.Y. Copper isotopic signature of the Tiegelongnan high-sulfidation copper deposit, Tibet: Implications for its origin and mineral exploration. *Miner. Depos.* **2016**, *51*, 591–602. [CrossRef]
34. Yang, H.H.; Tang, J.X.; Song, Y.; Wang, Q.; Liu, Z.B. The preservation mechanism of the Duolong ore district in northwest Tibet: Evidence from the low temperature thermochronological study. *Ore Geol. Rev.* **2022**, *143*, 104766. [CrossRef]
35. Li, J.X.; Qin, K.Z.; Li, G.M.; Xiao, B.; Zhao, J.X.; Chen, L. Magmatic-hydrothermal evolution of the cretaceous Duolong gold-rich porphyry copper deposit in the Bangongco metallogenic belt, Tibet: Evidence from U-Pb and $^{40}Ar/^{39}Ar$ geochronology. *J. Asian Earth Sci.* **2011**, *41*, 525–536. [CrossRef]
36. Zhou, X.; Fei, G.C.; Zhou, Y.; Wen, C.Q.; Zhang, Y.; Yue, X.Y. Chronology and crust-mantle mixing of ore-forming porphyry of the Bangongco: Evidence from zircon U-Pb age and Hf isotopes of the Naruo porphyry copper-gold deposit. *Acta Geol. Sin. Engl. Ed.* **2015**, *89*, 217–228.
37. Sun, J.; Mao, J.W.; Lin, B.; Yao, F.J.; Li, Y.B.; He, W.; Liu, Z.Q. Comparison of ore geology and ore-forming processes of ore deposits (ore spots) in Duolong area, Tibet. *Miner. Depos.* **2019**, *38*, 1159–1184. (In Chinese)
38. Yang, Y.; Zhang, Z.; Tang, J.X.; Chen, Y.C.; Li, Y.B.; Wang, L.Q.; Li, J.L.; Gao, K.; Wang, Q.; Yang, H.H. Mineralization, alteration and vein systems of the Bolong porphyry copper deposit in the Duolong ore concentration area, Tibet. *Geol. China* **2015**, *42*, 759–776. (In Chinese)
39. Li, G.M.; Zhang, X.N.; Qin, K.Z.; Sun, X.G.; Zhao, J.X.; Yin, X.B.; Li, J.X.; Yuan, H.S. The telescoped porphyry-high sulfidation epithermal Cu(-Au) mineralization of Rongna deposit in Duolong ore cluster at the southern margin of Qiangtang Terrane, Central Tibet: Integrated evidence from geology, hydrothermal alteration and sulfide assemblages. *Acta Petrol. Sin.* **2015**, *31*, 2307–2324. (In Chinese)
40. Wei, S.G.; Song, Y.; Tang, J.X.; Gao, K.; Feng, J.; Li, Y.B.; Hou, L. Geochronology, geochemistry and petrogenesis of quartz diorite porphyrite from the Sena copper (gold) deposit, Tibet. *Geol. China* **2016**, *43*, 1894–1912. (In Chinese)
41. Li, X.K.; Li, C.; Sun, Z.M.; Wu, H. Zircon U-Pb geochronology, Hf isotope, and whole-rock geochemistry of diorite in the Saijiao Cu-Au deposit, Tibet, and its ore-forming significance. *Geol. Bull. China* **2015**, *34*, 908–918. (In Chinese)
42. Sun, H.; Song, Y.; Li, F.Q.; Li, Z.C.; Wang, X.; Li, Y.; Zheng, M.; Fang, Y. Gaerqin deposit in Duolong ore district, Tibet: An epithermal gold deposit that suffered from erosion. *Miner. Depos.* **2023**, *42*, 287–309. (In Chinese)
43. He, Y.T.; Duan, C.; Hou, K.J.; Kong, Z.G.; Yuan, S.D.; Wang, C.L.; Yang, B.Y.; Yang, X.F.; Che, X.L.; Zhang, J.X.; et al. Trace Element Characteristics of Magnetite and Hematite from the Heshangqiao Iron Oxide–Apatite Deposit in Eastern China: Implications for the Ore-Forming Processes. *Minerals* **2026**, *16*, 7. [CrossRef]
44. Paton, C.; Hellstrom, J.; Paul, B.; Woodhead, J.; Hergt, J. Iolite: Freeware for the visualisation and processing of mass spectrometric data. *J. Anal. At. Spectrom.* **2011**, *26*, 2508. [CrossRef]
45. Chen, G.Y. Genetic Mineralogy: Its Development and Status Quo. *Geol. Explor.* **1987**, 26–29. (In Chinese)
46. Lin, S.Z. A Contribution to the Chemistry, Origin and Evolution of Magnetite. *Acta Mineral. Sin.* **1982**, 166–174. (In Chinese)
47. Wu, C.; Chen, H.Y.; Hong, W.; Li, D.F.; Liang, P.; Fang, J.; Zhang, L.J.; Lai, C. Magnetite chemistry and implications for the magmatic-hydrothermal ore-forming process: An example from the devonian yuleken porphyry Cu system, NW China. *Chem. Geol.* **2019**, *522*, 1–15. [CrossRef]
48. Xu, G.F.; Shao, J.L. Typomorphic Characteristics of Magnetite and Their Practical Significance. *Geol. Explor.* **1979**, 30–37. (In Chinese)
49. Nadoll, P.; Mauk, J.L.; Hayes, T.S.; Koenig, A.E.; Box, S.E. Geochemistry of magnetite from hydrothermal ore deposits and host rocks of the mesoproterozoic belt supergroup, united states. *Econ. Geol.* **2012**, *107*, 1275–1292. [CrossRef]
50. Sievwright, R.H.; Wilkinson, J.J.; O'Neill, H.S.C.; Berry, A.J. Thermodynamic controls on element partitioning between titanomagnetite and andesitic–dacitic silicate melts. *Contrib. Mineral. Petrol.* **2017**, *172*, 62. [CrossRef]
51. Deditius, A.P.; Reich, M.; Simon, A.C.; Suvorova, A.; Knipping, J.; Roberts, M.P.; Rubanov, S.; Saunders, M. Nanogeo chemistry of hydrothermal magnetite. *Contrib. Mineral. Petrol.* **2018**, *173*, 46. [CrossRef]
52. Carew, M.J.; Mark, G.; Oliver, N.H.S.; Pearson, N. Trace element geochemistry of magnetite and pyrite in Fe oxide (±Cu–Au) mineralised systems: Insights into the geochemistry of ore-forming fluids. *Geochim. Cosmochim. Acta* **2006**, *70*, A83. [CrossRef]
53. Toplis, M.J.; Corgne, A. An experimental study of element partitioning between magnetite, clinopyroxene and iron-bearing silicate liquids with particular emphasis on vanadium. *Contrib. Mineral. Petrol.* **2002**, *144*, 22–37. [CrossRef]

54. Balan, E.; De Villiers, J.P.; Eeckhout, S.G.; Glatzel, P.; Toplis, M.J.; Fristch, E.; Allard, T.; Galoisy, L.; Calas, G. The oxidation state of vanadium in titanomagnetite from layered basic intrusions. *Am. Mineral.* **2006**, *91*, 953–956. [CrossRef]
55. Sun, W.D.; Liang, H.Y.; Ling, M.X.; Zhang, M.Z.; Ding, X.; Zhang, H.; Yang, X.Y.; Li, Y.L.; Ireland, T.R.; Wei, Q.R.; et al. The link between reduced porphyry copper deposits and oxidized magmas. *Geochim. Cosmochim. Acta* **2013**, *103*, 263–275. [CrossRef]
56. Chen, W.T.; Zhou, M.F.; Gao, J.F.; Hu, R.Z. Geochemistry of magnetite from proterozoic Fe-Cu deposits in the kangdian metallogenic province, SW China. *Miner. Depos.* **2015**, *50*, 795–809. [CrossRef]
57. Rudnick, R.L.; Fountain, D.M. Nature and composition of the continental crust: A lower crustal perspective. *Rev. Geophys.* **1995**, *33*, 267–309. [CrossRef]
58. Ma, D. *Mineralogical Study of Magnetite in Xiongcun Copper (Gold) District, Tibet*; China University of Geosciences: Beijing, China, 2020. (In Chinese)

Disclaimer/Publisher's Note: The statements, opinions and data contained in all publications are solely those of the individual author(s) and contributor(s) and not of MDPI and/or the editor(s). MDPI and/or the editor(s) disclaim responsibility for any injury to people or property resulting from any ideas, methods, instructions or products referred to in the content.